

Dynamical study of $\pi N \rightarrow \pi\pi N$ reactions revisited

H. Kamano¹ and T.-S. H. Lee^{2,*}

¹*Research Center for Nuclear Physics,*

The University of Osaka, Ibaraki, Osaka 567-0047, Japan

²*Physics Division, Argonne National Laboratory, Argonne, Illinois 60439, USA*

Abstract

Using the Argonne National Laboratory-The University of Osaka (ANL-Osaka) DCC model of meson-nucleon reactions, we extend the study of Phys. Rev. C **79**, 025206 (2009) and Phys. Rev. C **88**, 045203 (2013) to predict the cross sections of the $\pi N \rightarrow \pi\pi N$ reactions. The model was constructed by fitting only the two-body reactions: $\pi N, \gamma N \rightarrow \pi N, \eta N, K\Lambda, K\Sigma$. Thus, the results for $\pi N \rightarrow \pi\pi N$ presented here are predictions of the ANL-Osaka DCC model, which serve to examine the extent to which the forthcoming data from J-PARC can be described. This study provides information for improving the extraction of nucleon resonances that have large decay widths to $\pi\pi N$ states. We present results for the total cross sections, invariant mass distributions, and angular distributions. We also identify the observables and energy regions where the higher mass nucleon resonances in the $S_{31}, P_{33}, D_{33}, F_{37}, D_{13}, D_{15}$, and F_{15} partial waves can be most effectively investigated.

PACS numbers: 13.60.Le, 14.20.Gk

* tshlee@anl.gov

I. INTRODUCTION

Recent studies employing coupled-channel approaches have greatly advanced our understanding of nucleon resonances (N^*)¹ (see, e.g., Ref. [1]). However, significant discrepancies among the results reported by various analysis groups remain to be resolved. These discrepancies are primarily observed for N^* states in the energy region where two-pion production dominates the πN reaction cross sections. For such N^* states, coupled-channel effects arising from three-body $\pi\pi N$ scattering states are expected to have a significant impact on their properties. Therefore, a comprehensive coupled-channel analysis that incorporates two-pion production data is indispensable for determining the properties of these N^* states.

Despite the importance of two-pion production data for firmly establishing N^* states, high-statistics data for the $\pi N \rightarrow \pi\pi N$ reaction suitable for detailed partial-wave analysis remain limited. Notable examples of precise measurements include the $\pi^- p \rightarrow \pi^0 \pi^0 n$ data obtained by Crystal Ball in 2004 [2], and more recently, the $\pi^- p \rightarrow \pi^- \pi^0 p$ and $\pi^- p \rightarrow \pi^+ \pi^- p$ measurements by HADES in 2020 [3]. These data have been incorporated in a recent partial-wave analysis [4]. However, these experiments were limited to relatively low energies ($W \lesssim 1.55$ GeV). Therefore, it is highly desirable to obtain such high-statistics data over the wide energy range up to $W \sim 2$ GeV. In this regards, the upcoming experiment at J-PARC [5] is expected to address this need. In this experiment, it is planned to measure the four reaction channels: $\pi^+ p \rightarrow \pi^+ \pi^+ n$, $\pi^+ p \rightarrow \pi^+ \pi^0 p$, $\pi^- p \rightarrow \pi^+ \pi^- n$, and $\pi^- p \rightarrow \pi^- \pi^0 p$. Also, the beam momenta used in the first measurement is planned to be 0.98–1.15 GeV/c, which corresponds to $W = 1.66$ –1.76 GeV. The J-PARC experiment aims at both of the $\pi^+ p$ and $\pi^- p$ reactions, and covers a higher energy region than those of Crystal Ball and HADES.

Given the importance of two-pion production processes in establishing N^* states, we have investigated the $\pi N \rightarrow \pi\pi N$ reactions in a series of works based on a dynamical coupled-channel (DCC) model, the Argonne National Laboratory-The University of Osaka (ANL-Osaka) DCC model [6–20]. Our first investigation of the $\pi N \rightarrow \pi\pi N$ reactions [9] employed the DCC model developed in Ref. [8]. This model incorporated five reaction channels (πN , ηN , and the three quasi-two-body channels of $\pi\pi N$: $\pi\Delta$, ρN , and σN), and the model parameters were determined by fitting to the SAID amplitudes [21] of πN elastic scattering up to $W = 2$ GeV. The model predicted the total cross sections and invariant mass distributions for $\pi N \rightarrow \pi\pi N$, describing the existing data reasonably well over a wide energy range from the threshold up to $W = 2$ GeV. It clearly demonstrated the critical role of unitarized coupled-channel effects in comprehensively describing πN reactions with various final states. In Ref. [14], we further investigate the $\pi N \rightarrow \pi\pi N$ reactions using the DCC model published in 2013 [13]. The 2013 model incorporated seven reaction channels (πN , ηN , $K\Lambda$, $K\Sigma$, $\pi\Delta$, ρN , and σN), and the model parameters were determined by fitting to the existing data for $\pi N \rightarrow \pi N, \eta N, K\Lambda, K\Sigma$ and $\gamma p \rightarrow \pi N, \eta N, K\Lambda, K\Sigma$ up to $W = 2$ GeV. This investigation particularly focused on clarifying the ambiguities in the N^* resonance parameters that arise when performing a comprehensive coupled-channel analysis excluding the $\pi N \rightarrow \pi\pi N$ data. The examination presented in Sec. IV of Ref. [14] showed that the coupled-channel analysis without the $\pi N \rightarrow \pi\pi N$ data indeed leaves sizable ambiguities in the N^* parameters, particularly those associated with the three-body $\pi\pi N$ channel. This indicates that the $\pi N \rightarrow \pi\pi N$ data are crucial for resolving these ambiguities.

Motivated by the activities of recent and upcoming experiments regarding the $\pi N \rightarrow \pi\pi N$ reactions mentioned above, in this work we extend our previous studies [9, 14] to further

¹ Unless otherwise specified, N^* refers to isospin $I = 1/2$ nucleon resonances and $I = 3/2$ Δ resonances.

investigate the potential impact of $\pi N \rightarrow \pi\pi N$ data on the determination of N^* parameters. As a primary objective, we examine the sensitivity of the N^* states to the $\pi N \rightarrow \pi\pi N$ cross sections, thereby providing useful information for the upcoming experiment at J-PARC. For this purpose, we employ the ANL-Osaka DCC model published in 2016 [16] (hereafter referred to as the 2016 model). This model extends the 2013 model by including $\gamma n \rightarrow \pi N$ data in the fit, and provides a superior description of the data for $\pi N \rightarrow \pi N, \eta N, K\Lambda, K\Sigma$ and $\gamma p \rightarrow \pi N, \eta N, K\Lambda, K\Sigma$.

In principle, one could also utilize $\gamma^{(*)} N \rightarrow \pi\pi N$ data to investigate two-pion production off the nucleon. However, describing photoproduction processes introduces additional model parameters associated with the electromagnetic interaction. Some of these parameters are sensitive specifically to the $\gamma N \rightarrow \pi\pi N$ reaction and are difficult to determine using only single-meson photoproduction data. Furthermore, from a technical standpoint, the computation of $\gamma N \rightarrow \pi\pi N$ observables is computationally quite demanding within DCC approaches. Therefore, data from purely hadronic $\pi N \rightarrow \pi\pi N$ processes are highly desirable as a first step to clarify the effects of reaction dynamics associated with the three-body $\pi\pi N$ channel on N^* states.

It is useful to briefly review the ANL-Osaka DCC model. Here we focus on hadronic reactions. This model is based on the meson-exchange mechanisms and the assumption that the (bare) N^* states emerge through the $\alpha \rightarrow N^*$ vertex interactions where α is the meson-baryon states with strangeness $S = 0$. Within the Hamiltonian formulation [6, 7], the unitary condition requires that the partial-wave amplitudes $T_{\beta,\alpha}(p_\beta, p_\alpha; W)$, which are specified by the total angular momentum J , parity P , and total isospin I (these indices are suppressed here), are given by the following coupled-channel equations:

$$T_{\beta,\alpha}(p_\beta, p_\alpha; W) = V_{\beta,\alpha}(p_\beta, p_\alpha; W) + \sum_\gamma \int p^2 dp V_{\beta,\gamma}(p_\beta, p; W) G_\gamma(p; W) T_{\gamma,\alpha}(p, p_\alpha; W), \quad (1)$$

with

$$V_{\beta,\alpha}(p_\beta, p_\alpha; W) = v_{\beta,\alpha}(p_\beta, p_\alpha) + Z_{\beta,\alpha}(p_\beta, p_\alpha; W) + \sum_{N^*} \frac{\Gamma_{N^*,\beta}^\dagger(p_\beta) \Gamma_{N^*,\alpha}(p_\alpha)}{W - M_{N^*}^0}, \quad (2)$$

where $\alpha, \beta, \gamma = \pi N, \eta N, \pi\Delta, \sigma N, \rho N, K\Lambda, K\Sigma$; $G_\gamma(p; W)$ is the Green's function of the channel γ ; $M_{N^*}^0$ is the mass of the bare N^* state; $v_{\beta,\alpha}(p_\beta, p_\alpha)$ represents meson-exchange mechanisms derived from effective Lagrangians; the energy-dependent $Z_{\beta,\alpha}(p_\beta, p_\alpha; W)$ term is the one-particle potential that produces the three-body $\pi\pi N$ cut; and the vertex interaction $\Gamma_{N^*,\alpha}(p_\alpha)$ defines the $\alpha \rightarrow N^*$ transition. The model parameters contained in $V_{\beta,\alpha}(p_\beta, p_\alpha; W)$ are determined by fitting to the world data of πN and $\gamma^{(*)} N$ reactions, and the N^* parameters such as pole masses and residues of the amplitudes at the pole are then extracted by making the analytic continuation of $T_{\beta,\alpha}(p_\beta, p_\alpha; W)$ to the complex-energy plane.

This paper is organized as follows. In Sec. II, we present the formulas for calculating the cross sections of $\pi N \rightarrow \pi\pi N$ reactions within the ANL-Osaka DCC model. The results and discussions are given in Sec. III. The summary is given in Sec. IV.

II. FORMULATION

In this section, we present the formulas for calculating the cross sections for the $\pi N \rightarrow \pi\pi N$ reactions used in this paper.

A. Kinematics and cross sections

In the total center-of-mass (CM) frame, the momentum variables for the $2 \rightarrow 3$ reactions can be specified as

$$a(\vec{p}_a) + b(\vec{p}_b) \rightarrow c(\vec{p}_c) + d(\vec{p}_d) + e(\vec{p}_e), \quad (3)$$

where $\vec{p}_a + \vec{p}_b = \vec{p}_c + \vec{p}_d + \vec{p}_e = 0$. For later use, we introduce \vec{k} and \vec{k}' defined by $\vec{k} = \vec{p}_a = -\vec{p}_b$ and $\vec{k}' = \vec{p}_c + \vec{p}_d = -\vec{p}_e$, respectively. The magnitude of \vec{k} (denoted as k) is determined by the relation $W = E_a(k) + E_b(k)$, where W is the total scattering energy in the total CM frame and $E_a(k) = \sqrt{m_a^2 + k^2}$ is the relativistic energy for a particle a with mass m_a and momentum \vec{k} . Similarly, the magnitude of \vec{k}' (denoted as k') is given by $W = E_e(k') + E_{cd}(k')$, where $E_{cd}(k')$ is defined by $E_{cd}(k') = \sqrt{M_{cd}^2 + k'^2}$ with M_{cd} being the invariant mass of the c - d pair. In the case of $\pi N \rightarrow \pi\pi N$ reaction, (c, d, e) in the final state corresponds to any allowed charge states formed from two pions and one nucleon.

Following the convention of Goldberger and Watson [24], the total cross sections and unpolarized differential cross sections investigated in this work are given by

$$\sigma = \int_{m_c+m_d}^{W-m_e} dM_{cd} \frac{d\sigma}{dM_{cd}} = \int d\Omega_{k'} \frac{d\sigma}{d\Omega_{k'}}, \quad (4)$$

$$\frac{d\sigma}{dM_{cd}} = \int d\Omega_{k'} \frac{d\sigma}{dM_{cd} d\Omega_{k'}}, \quad (5)$$

$$\frac{d\sigma}{d\Omega_{k'}} = \int_{m_c+m_d}^{W-m_e} dM_{cd} \frac{d\sigma}{dM_{cd} d\Omega_{k'}}, \quad (6)$$

with

$$\frac{d\sigma}{dM_{cd} d\Omega_{k'}} = 16\pi^3 \frac{\rho_{ab}}{k^2} \int d\Omega_{k_{cd}} \frac{k_{cd} k'}{W} E_c(p_c) E_d(p_d) E_e(p_e) \overline{\sum_{\text{spins}}} |T|^2, \quad (7)$$

where Ω_p denotes the solid angle for the momentum \vec{p} ; $\rho_{ab} = \pi k E_a(k) E_b(k) / W$; k_{cd} is the magnitude of the relative momentum between c and d in the CM frame of the c - d pair, which is given by $M_{cd} = E_c(k_{cd}) + E_d(k_{cd})$; T is the T -matrix element for the reaction; and the symbol $\overline{\sum_{\text{spins}}}$ in Eq. (7) denotes a summation over all final spins and an average over initial spins.

B. T -matrix element for $\pi N \rightarrow \pi\pi N$ in the ANL-Osaka DCC model

In the framework of the ANL-Osaka DCC model [7, 9], the $\pi N \rightarrow \pi\pi N$ reaction is described by the diagrams depicted in Fig. 1. The full T -matrix element in Eq. (7) is expressed as:

$$T = T^{\text{dir}} + \sum_{MB=\pi\Delta, \sigma N, \rho N} T^{MB}, \quad (8)$$

with

$$T^{\text{dir}} = V_{\pi\pi N, \pi N} + \sum_{MB} V_{\pi\pi N, MB} G_{MB} T_{MB, \pi N}, \quad (9)$$

$$T^{\pi\Delta} = \Gamma_{\pi N, \Delta} G_{\pi\Delta} T_{\pi\Delta, \pi N}, \quad (10)$$

$$T^{\rho N} = \Gamma_{\pi\pi, \rho} G_{\rho N} T_{\rho N, \pi N}, \quad (11)$$

$$T^{\sigma N} = \Gamma_{\pi\pi, \sigma} G_{\sigma N} T_{\sigma N, \pi N}. \quad (12)$$

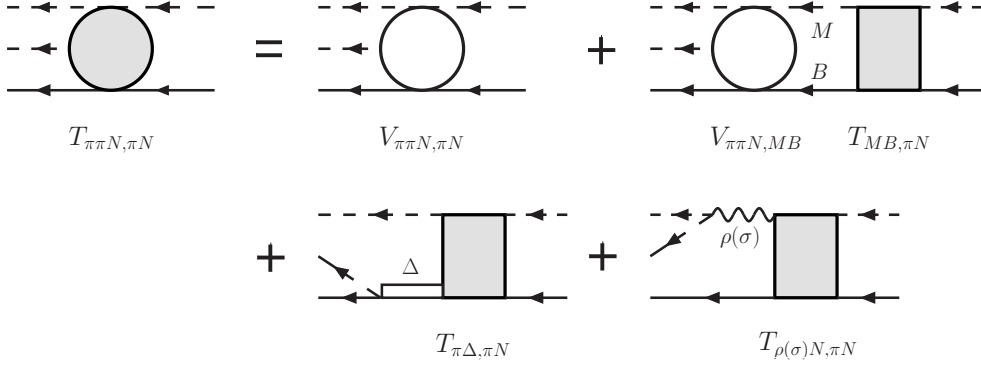


FIG. 1. Schematic representation of the $\pi N \rightarrow \pi\pi N$ reaction mechanisms. The figure is from Ref. [14].

In these expressions, $V_{\pi\pi N, MB}$ represents the potential for the direct transition from two-body to three-body states [9], while G_{MB} denotes the Green's function for the channel MB . The factors $\Gamma_{\pi N, \Delta}$, $\Gamma_{\pi\pi, \rho}$, and $\Gamma_{\pi\pi, \sigma}$ correspond to the decay vertices for $\Delta \rightarrow \pi N$, $\rho \rightarrow \pi\pi$, and $\sigma \rightarrow \pi\pi$, respectively. The summation over MB in Eq. (9) includes the channels $MB = \pi N, \eta N, \pi\Delta, \rho N, \sigma N, K\Lambda, K\Sigma$. We compute the two-body plane-wave amplitudes, $T_{MB, \pi N}$, from the partial-wave amplitudes derived by solving Eq. (1). For full details regarding the two-body amplitudes, meson-baryon Green's functions, and decay vertices, we refer the reader to Ref. [7, 9]. Concerning the direct term $T_{\pi\pi N, \pi N}^{\text{dir}}$, however, we implement the practical prescription given in Eq. (16) of Ref. [9], which simplifies the amplitude to:

$$T_{\pi\pi N, \pi N}^{\text{dir}} \sim \tilde{V}_{\pi\pi N, \pi N} + \Gamma_{\pi N, N} G_{\pi N} T_{\pi N, \pi N}. \quad (13)$$

Here, $\tilde{V}_{\pi\pi N, \pi N}$ denotes the direct $\pi N \rightarrow \pi\pi N$ transition potential associated with diagrams (f)-(k) in Fig. 2 of Ref. [9], and $\Gamma_{\pi N, N}$ is the $N \rightarrow \pi N$ vertex function.

III. RESULTS AND DISCUSSIONS

A. Total cross sections

Figure 2 shows the total cross sections for the $\pi N \rightarrow \pi\pi N$ reactions based on the predictions obtained with the 2016 model [16]. The predicted full result for the $\pi^+ p \rightarrow \pi^+ \pi^+ n$ reaction is found to be in good agreement with the existing data up to $W = 2$ GeV. For the other four reactions, our results show reasonable agreement with the data at low energies; however, they significantly overestimate the data above $W \sim 1.65$ GeV. This behavior is consistent with our previous results reported in 2013 [14]. In the same figure, we also show the contributions of each reaction process defined in Eq. (8) to the total cross sections. For the $\pi^+ p \rightarrow \pi^+ \pi^+ n$ reaction [Fig. 2(a)], only the isospin $I = 3/2$ components of $T^{\pi\Delta}$ and T^{dir} contribute, and these contributions are comparable over the entire energy range up to $W = 2$ GeV. On the other hand, contributions arise from the isospin $I = 3/2$ components of $T^{\pi\Delta}$, $T^{\rho N}$, and T^{dir} in the $\pi^+ p \rightarrow \pi^+ \pi^0 p$ reaction [Fig. 2(b)]. Given that the T^{dir} process gives a negligible contribution compared to the other two processes for this reaction, fine-tuning of the isospin $I = 3/2$ components of $T^{\pi\Delta}$ and $T^{\rho N}$ will be required to

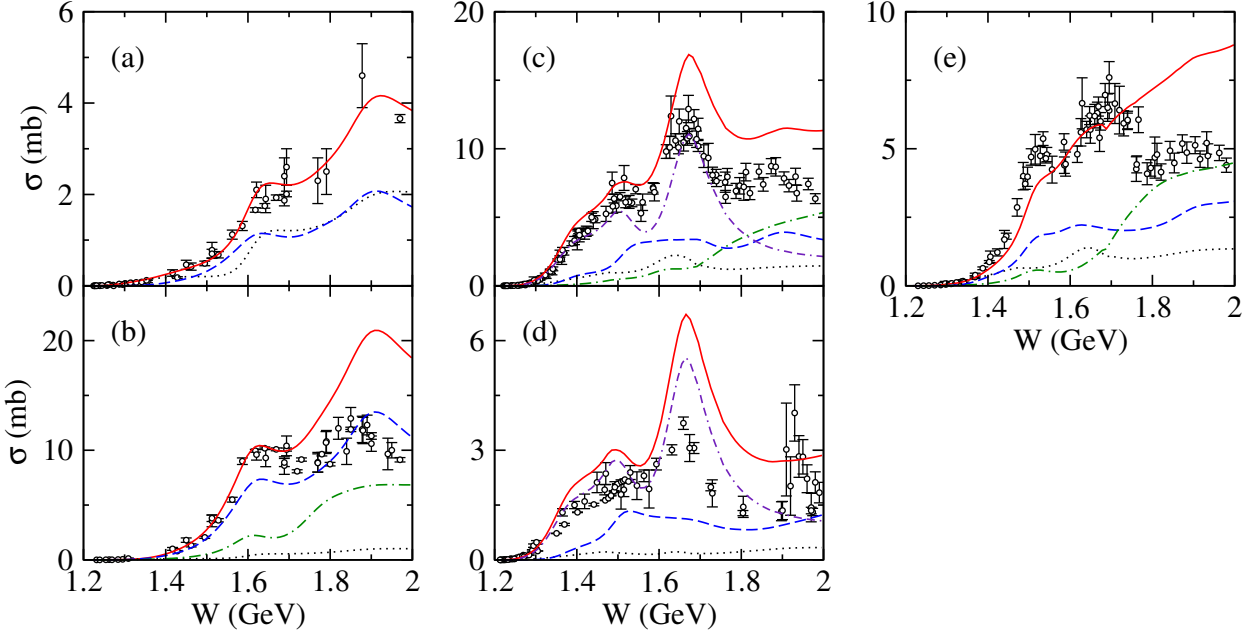


FIG. 2. Total cross sections of (a) $\pi^+ p \rightarrow \pi^+ \pi^+ n$, (b) $\pi^+ p \rightarrow \pi^+ \pi^0 n$, (c) $\pi^- p \rightarrow \pi^+ \pi^- n$, (d) $\pi^- p \rightarrow \pi^0 \pi^0 n$, and (e) $\pi^- p \rightarrow \pi^- \pi^0 p$. Solid (red) curves are the full results; dashed (blue) curves are the results of $T^{\pi\Delta}$ process only; dash-dot (green) curves are the results of $T^{\rho N}$ process only; dash-dash-dot (indigo) curves are the results of $T^{\sigma N}$ process only; and dotted (black) curves are the results of T^{dir} process only. See Refs. [9, 22] and references therein for the data.

resolve the significant overestimation of the total cross sections above $W \sim 1.7$ GeV. For the $\pi^- p \rightarrow \pi^+ \pi^- n$ and $\pi^- p \rightarrow \pi^0 \pi^0 n$ reactions [Fig. 2(c) and (d)], the $T^{\sigma N}$ process dominates the cross sections at low energies and is responsible for the peak at $W \sim 1.65$ GeV. Contributions from the $T^{\pi\Delta}$ and $T^{\rho N}$ processes are also non-negligible and become comparable to those of $T^{\sigma N}$ above $W \sim 1.8$ GeV, while the T^{dir} process provides a minor contribution, particularly for $\pi^- p \rightarrow \pi^0 \pi^0 n$. The consistent overestimation of these cross sections up to $W = 2$ GeV suggests that the decays of $I = 1/2$ N^* states to $\pi\Delta$, ρN , and σN in particular are poorly constrained by the partial-wave analysis of single-meson production alone. Consequently, incorporating $\pi N \rightarrow \pi\pi N$ data into the analysis is essential. For the $\pi^- p \rightarrow \pi^- \pi^0 p$ channel [Fig. 2(e)], the contributions from $T^{\pi\Delta}$, $T^{\rho N}$ and T^{dir} are of comparable magnitude throughout the energy range up to $W = 2$ GeV. Resolving the overestimation above $W \sim 1.8$ GeV necessitates refinements to all three processes. We also note that a small cusp structure appears at $W \sim 1.68$ GeV in the $\pi^- p \rightarrow \pi^- \pi^0 p$ total cross section. This behavior is attributed to the opening of the $K\Sigma$ channel and arises from the S -wave $\pi N \rightarrow \rho N$ amplitude in $T^{\rho N}$.

Figures 3 and 4 show the partial-wave contributions to the total cross sections up to $J = 9/2$. Generally, the behavior of each partial wave is consistent with our previous results based on the 2013 model [13]. Regarding the initial $\pi^+ p$ reactions [Fig. 3], the P_{33} partial wave dominates the $\pi^+ p \rightarrow \pi^+ \pi^+ n$ cross section from the threshold to $W = 1.4$ GeV, while several partial waves contribute comparably to $\pi^+ p \rightarrow \pi^+ \pi^0 n$ at low energies. In the $W = 1.5$ – 1.75 GeV region, however, S_{31} and D_{33} dominate both reactions, with F_{37} taking over above $W = 1.8$ GeV. For the initial $\pi^- p$ reactions [Fig. 4], $I = 3/2$ partial

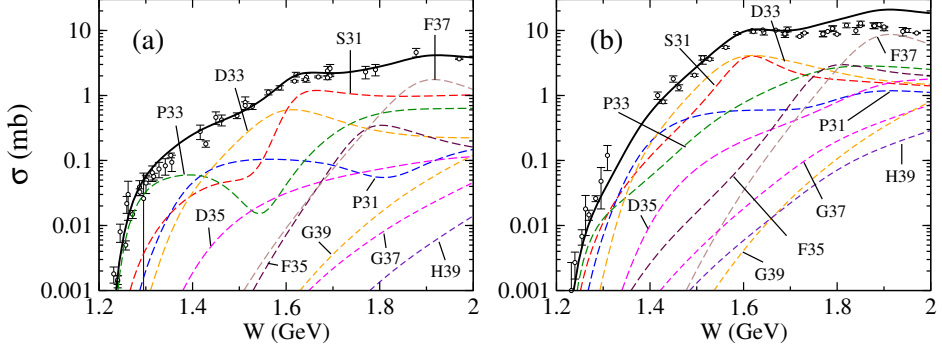


FIG. 3. Contribution of each partial wave to the $\pi^+ p \rightarrow \pi\pi N$ total cross sections: (a) $\pi^+ p \rightarrow \pi^+ \pi^+ n$ and (b) $\pi^+ p \rightarrow \pi^+ \pi^0 p$. Solid curves are the full results, while dashed curves are contributions of each partial wave to the cross sections. See Refs. [9, 22] and references therein for the data.

waves represent sub-dominant contributions, except in the $\pi^+ \pi^- n$ and $\pi^- \pi^0 p$ final states at $W \sim 1.9$ GeV, where F_{37} is comparable to the largest $I = 1/2$ waves. Between $W = 1.5$ and 1.75 GeV, D_{13} and D_{15} are dominant in all three charged states, as is F_{15} for the $\pi^+ \pi^- n$ and $\pi^0 \pi^0 n$ final states. We emphasize that the P_{11} partial wave dominates the $\pi^- p \rightarrow \pi^+ \pi^- n$ and $\pi^- p \rightarrow \pi^0 \pi^0 n$ up to $W \sim 1.4$ GeV, corresponding to the Roper resonance region. As mentioned in Ref. [14], this contrasts with photoproduction, where the Roper resonance makes a minor contribution and is overshadowed by the prominent first D_{13} resonance. Thus $\pi N \rightarrow \pi\pi N$ reactions offer crucial insights into high-mass N^* states and the elusive Roper resonance.

B. Invariant mass distributions and angular distributions

In this subsection, we present our predictions for invariant mass distributions and angular distributions from the 2016 model. First we focus on the low energy region below $W = 1.55$ GeV, where the precise data for $\pi^- p \rightarrow \pi\pi N$ from Crystal Ball and HADES are available.

Figures 5 and 6 compare our predictions with the HADES data at $W = 1487$ MeV. HADES provides the data for the $\pi^- p \rightarrow \pi^+ \pi^- n$ and $\pi^- p \rightarrow \pi^- \pi^0 p$ reactions. We observe that the predicted invariant mass distributions for $\pi^- p \rightarrow \pi^+ \pi^- n$ show significant deviations from the data, as seen in Fig. 5 (a) and (b). As demonstrated in Refs. [25, 26], strong interference between $T^{\pi\Delta}$ and $T^{\sigma N}$ is crucial for describing the shape of the invariant mass distributions for $\pi^- p \rightarrow \pi^+ \pi^- n$ and $\pi^- p \rightarrow \pi^0 \pi^0 n$ in the Roper resonance region. Since the predicted invariant mass distributions are largely governed by the behavior of the $T^{\sigma N}$ process, the observed discrepancy implies that the $N^* \rightarrow \pi\Delta$ decay is underestimated and/or the $N^* \rightarrow \sigma N$ decay is overestimated in the 2016 model. This discrepancy is corroborated by the angular distributions of $\pi^- p \rightarrow \pi^+ \pi^- n$ [Fig. 6 (a) and (b)], where the predictions exhibit a significantly different angular dependence compared to the data. Thus, the HADES data for $\pi^- p \rightarrow \pi^+ \pi^- n$ provide crucial constraints for determining the $\pi\Delta$ and σN couplings to N^* in the Roper resonance region. For the $\pi^- p \rightarrow \pi^- \pi^0 p$ reaction, our predictions reproduce the general trends of the data. However, discrepancies appear in the high invariant-mass

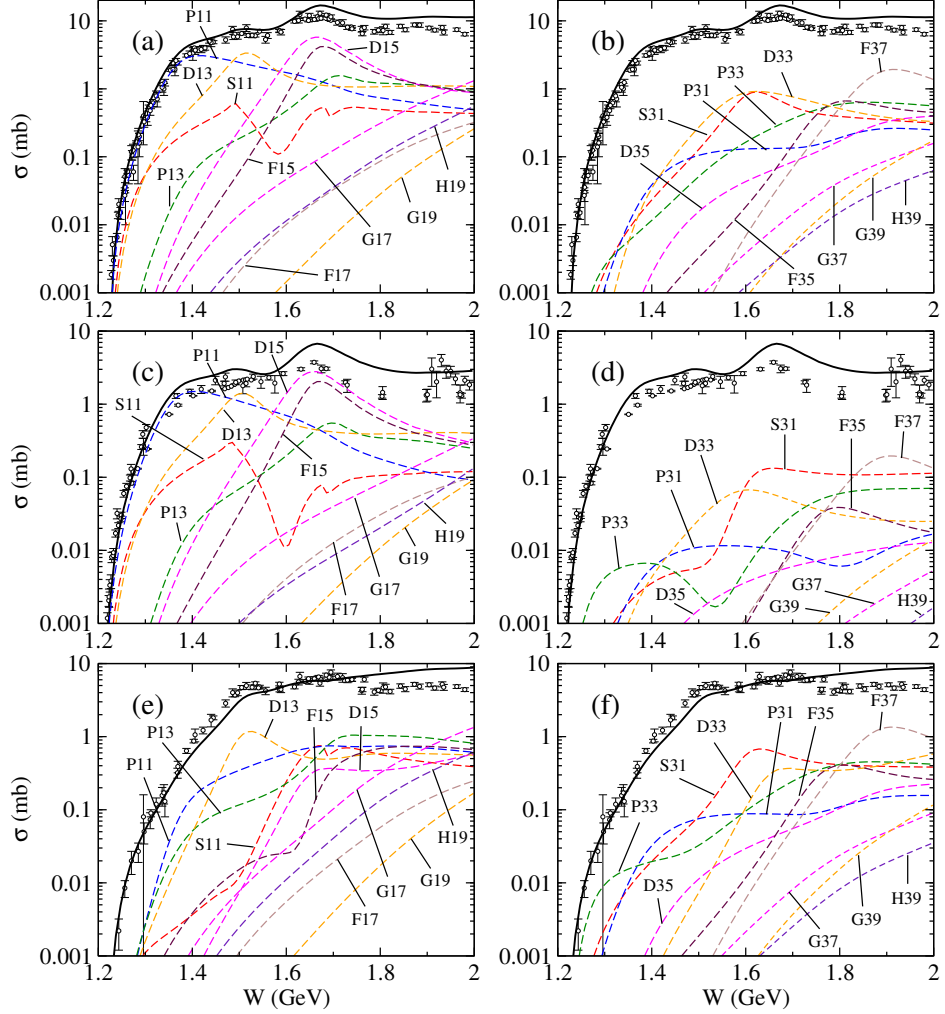


FIG. 4. Contribution of each partial wave to the $\pi^-p \rightarrow \pi\pi N$ total cross sections. Panels (a) and (b) $\pi^-p \rightarrow \pi^+\pi^-n$, (c) and (d) $\pi^-p \rightarrow \pi^0\pi^0n$, and (e) and (f) $\pi^-p \rightarrow \pi^-\pi^0p$. Panels (a), (c), and (e) [(b), (d), and (f)] present $I = 1/2$ [$I = 3/2$] partial waves. Solid curves are the full results, while dashed curves are contributions of each partial wave to the cross sections. See Refs. [9, 22] and references therein for the data.

region of the invariant mass distributions [Fig. 5 (c) and (d)] and in the angular distributions at $\cos\theta_p \gtrsim 0$ [Fig. 6 (c)] and around $\cos\theta_{\pi^0} \sim 0$ [Fig. 6 (d)]. Although $T^{\pi\Delta}$ is dominant, the contributions from $T^{\rho N}$ and T^{dir} are non-negligible. Fine-tuning these three processes will be required to better describe the data.

Figure 7 shows the comparison with the angular distribution data for $\pi^-p \rightarrow \pi^0\pi^0n$ from Crystal Ball, covering the energy range from near the threshold to $W \sim 1530$ MeV. Since neither $T^{\rho N}$ nor other $\pi N \rightarrow MN$ processes (where M is an unflavored $I = 1$ meson) contribute to this channel, this reaction is particularly useful for investigating the σN coupling to N^* . Similar to the case of $\pi^-p \rightarrow \pi^+\pi^-n$ [Fig. 6 (a) and (b)], where $T^{\sigma N}$ also contributes, a major source of the significant deviation from the data arises from the large contribution of the $T^{\sigma N}$ process. Adjusting the relative strength and interference between $T^{\sigma N}$ and the other processes will be key to resolving the discrepancies between our results and the data

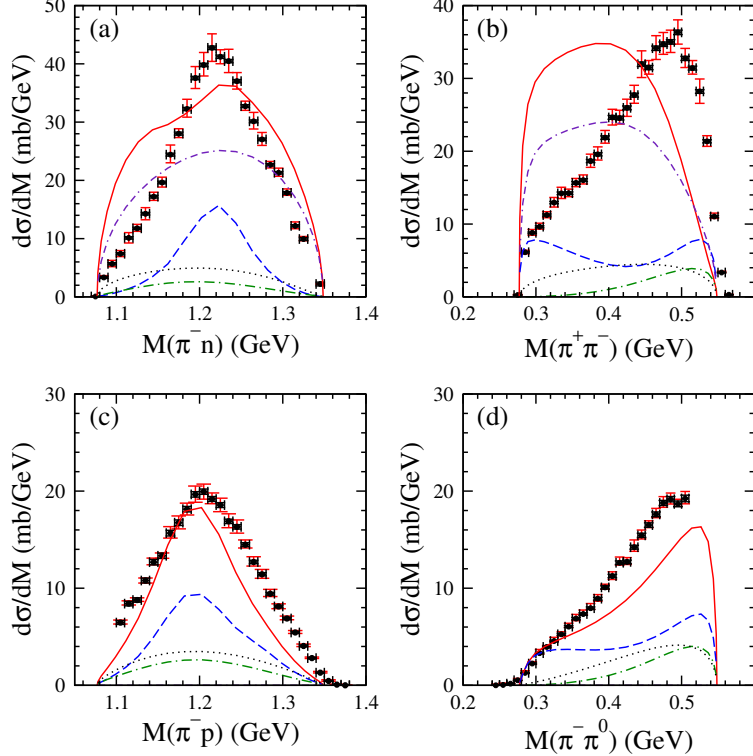


FIG. 5. Comparison with the HADES data [3] for the invariant mass distributions at $W = 1487$ MeV ($p_{\text{in}} = 685$ MeV/c with p_{in} being pion beam momenta). Panels (a) and (b) are of $\pi^-p \rightarrow \pi^+\pi^-n$, and panels (c) and (d) are of $\pi^-p \rightarrow \pi^-\pi^0p$. The meaning of each curve is the same as in Fig. 2

at forward and backward angles.

Although the existing data for $\pi^-p \rightarrow \pi\pi N$ from Crystal Ball and HADES are of particular interest in connection with the Roper resonance, we need precise differential cross section data in the higher energy region as well, in order to establish the high-mass N^* resonances where the double pion production dominates πN reactions. Furthermore, data for $\pi^+p \rightarrow \pi\pi N$ are highly desirable. Due to isospin filtering, the π^+p reactions provide an ideal platform to exclusively investigate the isospin $I = 3/2$ Δ^* resonances. The upcoming experiment at J-PARC offers a promising opportunity to address these issues. It is planned to utilize both π^- and π^+ beams to measure the reactions $\pi^-p \rightarrow \pi^+\pi^-n$, $\pi^-p \rightarrow \pi^-\pi^0p$, $\pi^+p \rightarrow \pi^+\pi^+n$, and $\pi^+p \rightarrow \pi^+\pi^0p$ in the energy region around $W = 1.7$ GeV [5]. In what follows, we present predictions based on our 2016 model for the invariant mass distributions within the energy region anticipated for this experiment.

Figures 8 and 9 show the invariant mass distributions for $\pi^+p \rightarrow \pi^+\pi^+n$ and $\pi^+p \rightarrow \pi^+\pi^0p$ in the higher energy region at $W = 1.54$, 1.7 , and 1.87 GeV, respectively. Our predictions reproduce the overall behavior of the existing histogram data [23] well, although they slightly (significantly) overestimate the data for $\pi^+p \rightarrow \pi^+\pi^+n$ ($\pi^+p \rightarrow \pi^+\pi^0p$) at $W = 1.7$ and 1.87 GeV. Since the $\pi N \rightarrow \pi N$ subprocess in T^{dir} [$T_{\pi N, \pi N}$ in the second term of Eq. (13)] is already well determined within our 2016 model, fine-tuning the $\Delta^* \rightarrow \pi\Delta$ vertex in $T^{\pi\Delta}$ will be required to reduce the predicted magnitudes and achieve a better

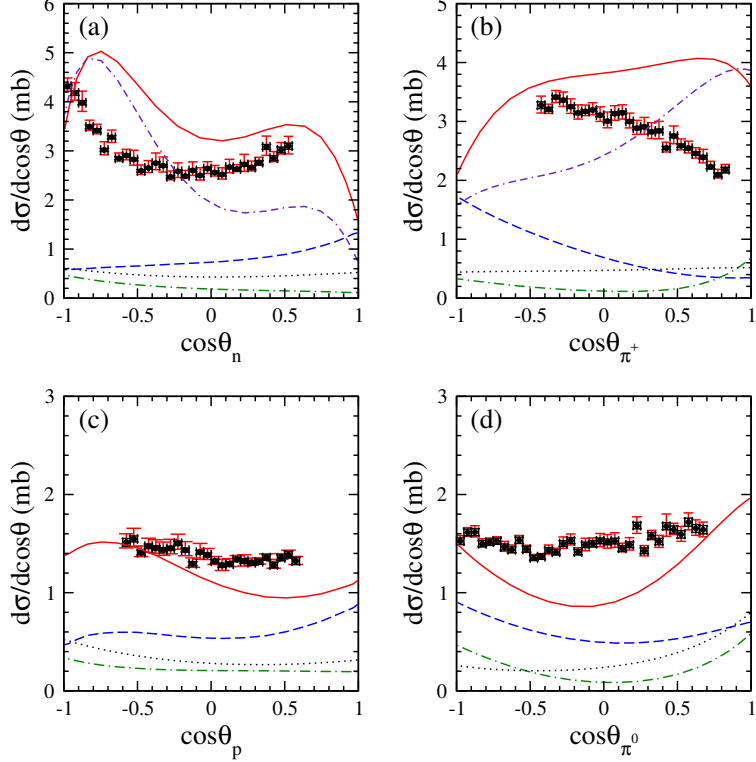


FIG. 6. Comparison with the HADES data [3] for the angular distributions at $W = 1487$ MeV ($p_{\text{in}} = 685$ MeV/c with p_{in} being pion beam momenta). Panels (a) and (b) are of $\pi^- p \rightarrow \pi^+ \pi^- n$, and panels (c) and (d) are of $\pi^- p \rightarrow \pi^- \pi^0 p$. The meaning of each curve is the same as in Fig. 2.

description of the data. This conclusion also holds for the $\pi^+ p \rightarrow \pi^+ \pi^0 p$ reaction.

Figures 10 and 11 show the invariant mass distributions for $\pi^- p \rightarrow \pi^+ \pi^- n$ and $\pi^- p \rightarrow \pi^- \pi^0 p$ at $W = 1.54$, 1.7 , and 1.87 GeV, respectively. In contrast to the $\pi^+ p \rightarrow \pi\pi N$ case, our results show discrepancies with the existing data not only in magnitude but also in shape. For $\pi^- p \rightarrow \pi^+ \pi^- n$, the major source of these discrepancies appears to be the large contribution from the $T^{\sigma N}$ process, implying that refinements to the $N^* \rightarrow \sigma N$ couplings are necessary. On the other hand, the $T^{\sigma N}$ process does not contribute to the $\pi^- p \rightarrow \pi^- \pi^0 p$ reaction; thus, fine-tuning of all involved processes ($T^{\pi\Delta}$, $T^{\rho N}$, and T^{dir}), including the interferences among them, will be required.

Figure 12 shows the invariant mass distributions for $\pi^- p \rightarrow \pi^0 \pi^0 n$ at $W = 1.54$, 1.7 , and 1.87 GeV. Although no data exist for this reaction at these energies, we anticipate that a similar argument to that for the $\pi^- p \rightarrow \pi^+ \pi^- n$ reaction discussed above applies here as well.

C. Sensitivity to the N^* states

We have seen from Figs. 2 and 8-11 that, in the energy region above $W \sim 1.65$ GeV, which lies beyond the range covered by the Crystal Ball and HADES experiments, significant discrepancies between our predictions and the existing data appear for all five reactions. This is mainly attributed to the fact that the $\pi\Delta$, ρN , and σN couplings to N^* are not well

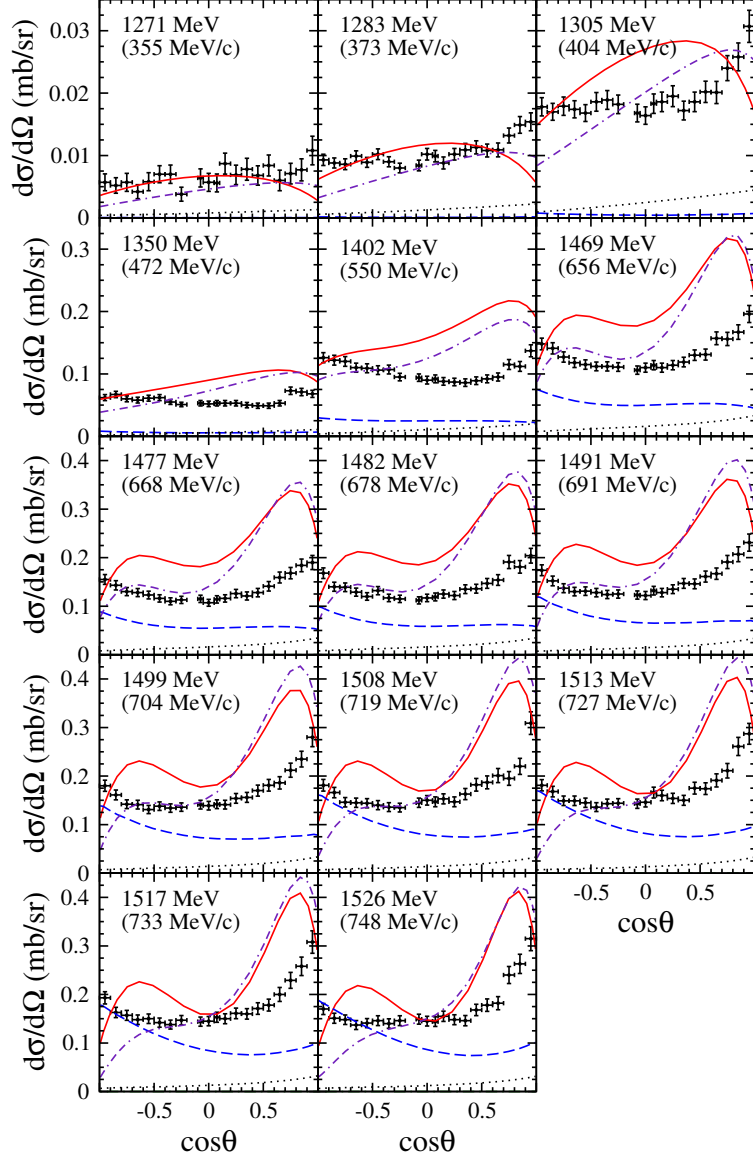


FIG. 7. Comparison with the Crystal Ball data [2] for the angular distributions of $\pi^- p \rightarrow \pi^0 \pi^0 n$. The solid angle Ω and scattering angle θ are of the outgoing $2\pi^0$ system. In each panel, the corresponding W (p_{in} in parenthesis) is presented. The meaning of each curve is the same as in Fig. 2.

determined by the data from single-meson production reactions that were included in the partial-wave analysis to construct our 2016 model.

In this subsection, we investigate the sensitivity of the observables to variations of the $\pi\Delta$, ρN , and σN couplings to N^* . Through this investigation, we aim to demonstrate which reaction channels, observables, and kinematics are useful for extracting N^* parameters, thereby providing valuable input for future experiments. To proceed, we adopt the following procedure:

1. Recall that, within the ANL-Osaka DCC model, the full partial-wave amplitude

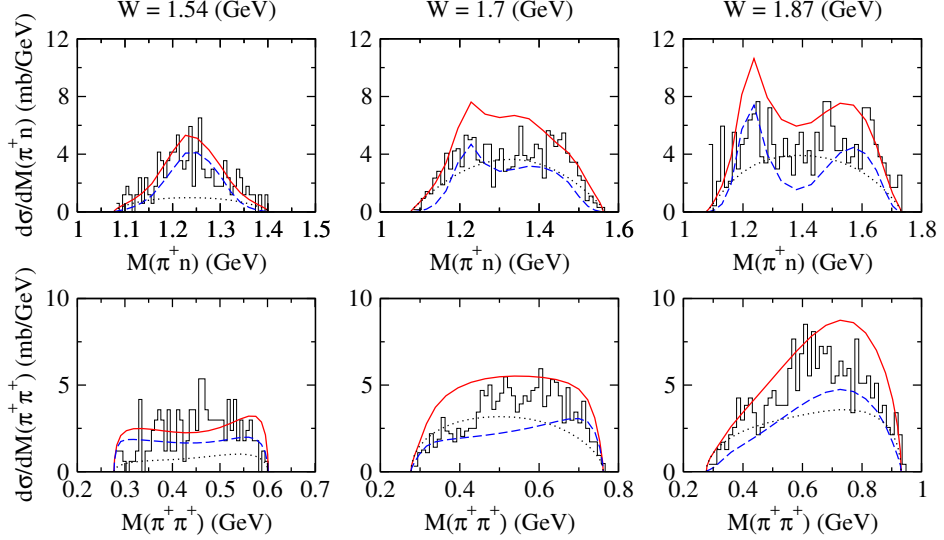


FIG. 8. Invariant mass distributions of $\pi^+ p \rightarrow \pi^+ \pi^+ n$ at $W = 1.54, 1.70$, and 1.87 GeV. The meaning of each curve is the same as in Fig. 2. The data are from Arndt [23].

[Eq. (1)] for $\pi N \rightarrow MB$ ($MB = \pi\Delta, \rho N, \sigma N$) for a given total isospin I , total spin J , and parity P can be expressed as a sum of non-resonant (t^{NR}) and resonant (t^{R}) amplitudes (here the energy and momentum indices are suppressed):

$$T_{MB(LS),\pi N} = t_{MB(LS),\pi N}^{\text{NR}} + t_{MB(LS),\pi N}^{\text{R}}, \quad (14)$$

where L and S represent the allowed total angular momentum and spin of the MB channel for a given (I, J, P) , respectively. The resonant amplitude t^{R} is given by

$$t_{MB(LS),\pi N}^{\text{R}} = \sum_{n,m} \bar{\Gamma}_{MB(LS),N_n^*} D_{n,m} \bar{\Gamma}_{N_m^*,\pi N}, \quad (15)$$

where the indices n, m specify the n -th and m -th bare N^* states with quantum numbers of (I, J, P) ; $\bar{\Gamma}_{MB(LS),N_n^*}$ ($\bar{\Gamma}_{N_m^*,\pi N}$) is the fully dressed vertex for the $N_n^* \rightarrow MB(LS)$ ($\pi N \rightarrow N_m^*$) transition; and $D_{n,m}$ is the dressed N^* propagator [13]. It is important to note that the dressed N^* propagator in the resonant amplitude t^{R} contains the poles of *physical* N^* resonances obtained by solving the full scattering equation [Eq. (1)], and that the fully dressed vertices evaluated at these pole energies can be associated with the “coupling strength” of the corresponding N^* resonances to the MB states.²

2. Multiply $\bar{\Gamma}_{MB(LS),N_n^*}$ by a common real factor $a_{MB(LS),N^*(I,J^P)}$ for all n to define a modified fully dressed vertex:

$$\bar{\Gamma}'_{MB(LS),N_n^*} \equiv a_{MB(LS),N^*(I,J^P)} \times \bar{\Gamma}_{MB(LS),N_n^*} \quad (\text{for all } n), \quad (16)$$

and replace $\bar{\Gamma}_{MB(LS),N_n^*}$ in the resonant amplitude t^{R} [Eq. (15)] with this modified one.

² Poles may be dynamically generated in t^{NR} through the infinite iteration of the non-resonant potentials [the first two terms on the right-hand side of Eq. (2)]. However, if the bare N^* states [the last term on the right-hand side of Eq. (2)] are added to the transition potential $V_{\beta,\alpha}$, the poles in t^{NR} and the bare N^* states play a qualitatively similar role: the mixing between the poles in t^{NR} and the bare N^* states results in the physical resonances.

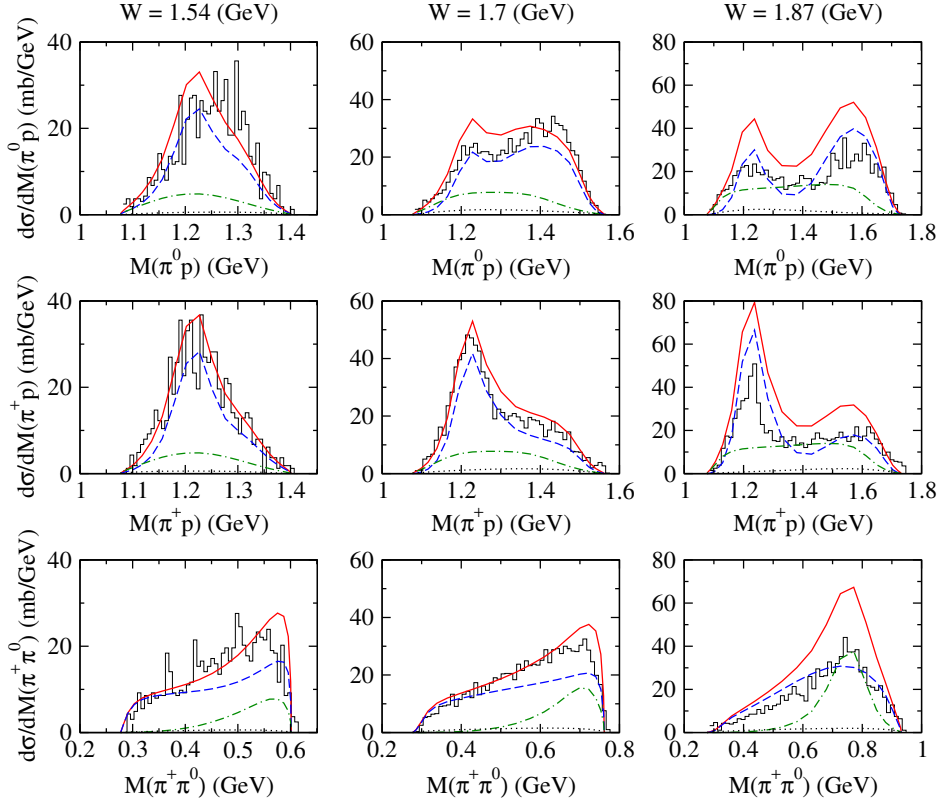


FIG. 9. Invariant mass distributions of $\pi^+p \rightarrow \pi^+\pi^0p$ at $W = 1.54, 1.70$, and 1.87 GeV. The meaning of each curve is the same as in Fig. 2. The data are from Arndt [23].

3. Compute the cross sections by varying $a_{MB(LS),N^*(I,J^P)}$ from 1 and examine how the cross sections change as $a_{MB(LS),N^*(I,J^P)}$ is varied.

The above procedure essentially corresponds to uniformly varying the magnitudes of the MB couplings to the physical N^* resonances within a given partial wave. This analysis serves to fulfill the objective described above.

In what follows, we investigate the sensitivity of the $\pi N \rightarrow \pi\pi N$ observables to the N^* resonances by examining the total cross sections [Eq. (4)] and invariant mass distributions [Eq. (5)]. The results for the angular distributions [Eq. (6)] are presented in Appendix A.

1. Isospin $I = 3/2$ Δ^*

We first investigate the sensitivity of the cross sections to the $I = 3/2$ Δ^* resonances. As we have seen from Figs. 3 and 4, above $W = 1.6$ GeV, S_{31} , P_{33} , D_{33} , and F_{37} have large contributions among the $I = 3/2$ partial waves.

S_{31} : Figures 13 and 14 show the sensitivity of the total cross sections and invariant mass distributions to the strengths of the dressed vertices for $S_{31}[\Delta^*(J^P = \frac{1}{2}^-)] \rightarrow \pi\Delta(L = 2, S = \frac{3}{2})$ and $S_{31}[\Delta^*(J^P = \frac{1}{2}^-)] \rightarrow \rho N(L = 0, S = \frac{1}{2})$, respectively. Here, we present results only for the reactions that are sensitive to the $\pm 50\%$ variation in the magnitudes of these vertices. Results for other dressed vertices are also omitted due to their negligible

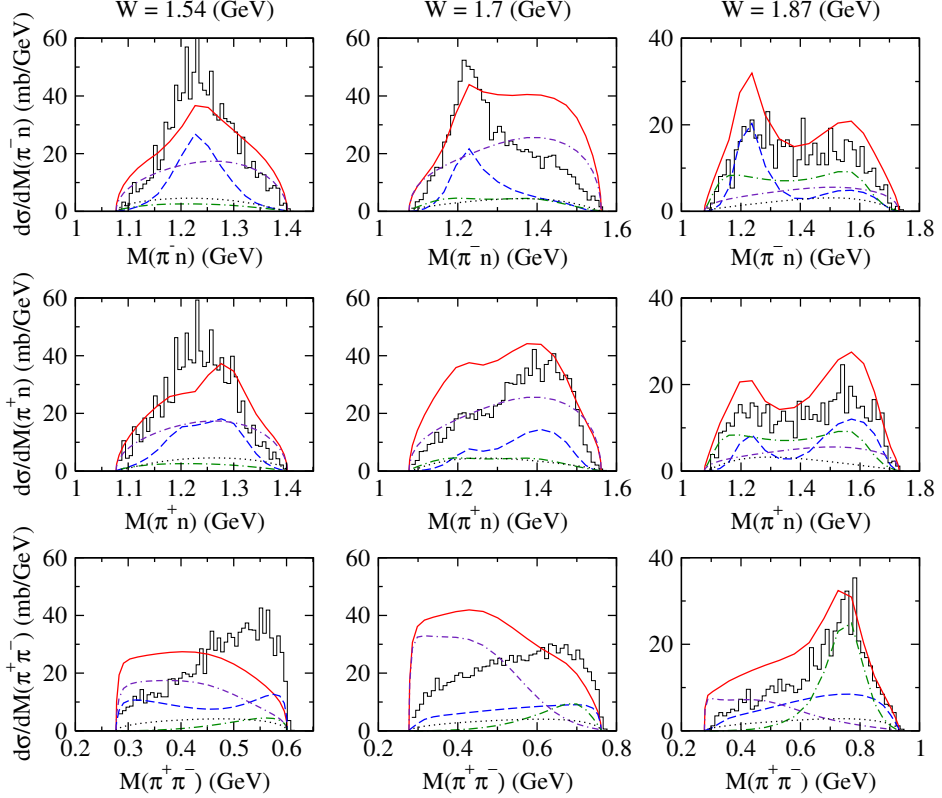


FIG. 10. Invariant mass distributions of $\pi^- p \rightarrow \pi^+ \pi^- n$ at $W = 1.54, 1.70$, and 1.87 GeV. The meaning of each curve is the same as in Fig. 2. The data are from Arndt [23].

sensitivity. (We apply this same criterion to the discussions of other partial waves below.) In the total cross sections, we observe that these variations have a significant effect at $W = 1.6$ – 1.7 GeV. This corresponds to the energy region where two resonances with pole masses of $1597 - i69$ MeV and $1713 - i187$ MeV are located in this partial wave within our 2016 model [16]. Regarding the invariant mass distributions at $W = 1.7$ GeV, the variation in the $S_{31}[\Delta^*(J^P = \frac{1}{2}^-)] \rightarrow \pi\Delta(L = 2, S = \frac{3}{2})$ vertex affects the $\pi^+ p \rightarrow \pi^+ \pi^+ n$ and $\pi^+ p \rightarrow \pi^+ \pi^0 p$ reactions uniformly over the entire kinematically allowed range. In contrast, the impact of the $S_{31}[\Delta^*(J^P = \frac{1}{2}^-)] \rightarrow \rho N(L = 0, S = \frac{1}{2})$ variation is generally small, although a significant effect is observed in the $\pi^+ \pi^0$ invariant mass distribution for the $\pi^+ p \rightarrow \pi^+ \pi^0 p$ reaction in the region of $M_{\pi\pi} \gtrsim 0.65$ GeV. A reduction in the magnitude of the $S_{31}[\Delta^*(J^P = \frac{1}{2}^-)] \rightarrow \rho N(L = 0, S = \frac{1}{2})$ vertex appears to be favored by the data.

P_{33} : Figure 15 shows the sensitivity of the total cross sections and invariant mass distributions to the strength of the dressed vertex for $P_{33}[\Delta^*(J^P = \frac{3}{2}^+)] \rightarrow \pi\Delta(L = 1, S = \frac{3}{2})$. A visible effect from the $\pm 50\%$ variation in the $P_{33}[\Delta^*(J^P = \frac{3}{2}^+)] \rightarrow \pi\Delta(L = 1, S = \frac{3}{2})$ vertex is observed in the total cross sections over a wide energy region above $W \sim 1.6$ GeV. However, this effect appears minor and is not sufficient to improve the description of the data. This behavior would be attributed to the broad P_{33} resonance with a pole mass of $1733 - i162$ MeV found in our 2016 model [16]. The influence on the invariant mass distributions at $W = 1.7$ GeV is also visible but minor.

D_{33} : Figure 16 shows the sensitivity of the total cross sections and invariant mass dis-

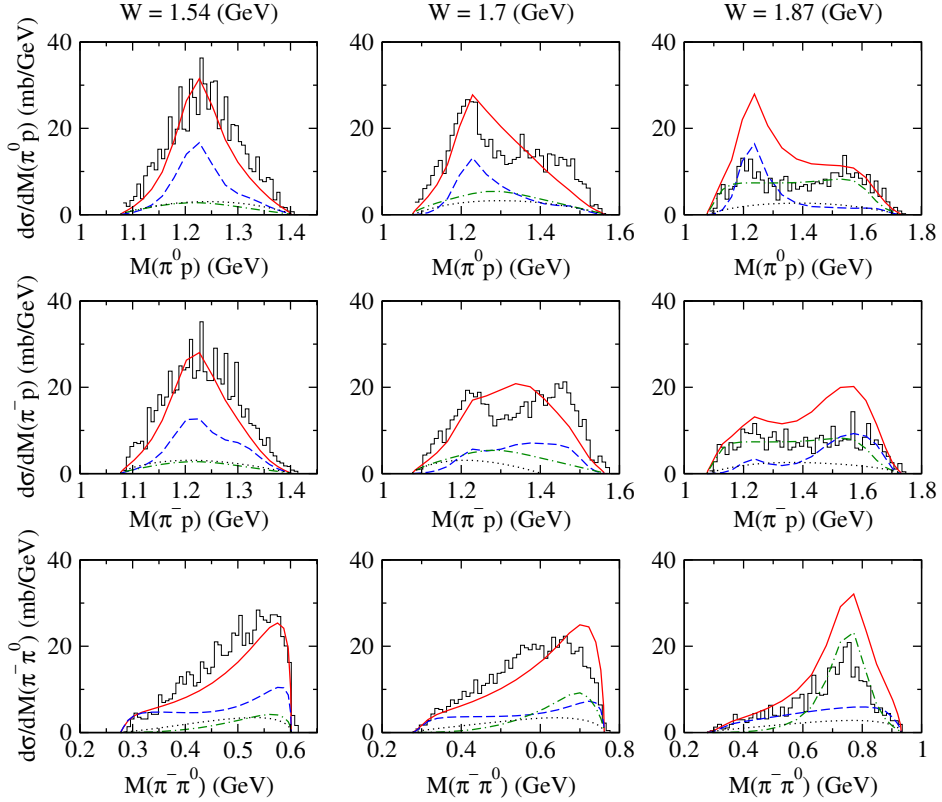


FIG. 11. Invariant mass distributions of $\pi^- p \rightarrow \pi^- \pi^0 p$ at $W = 1.54, 1.70$, and 1.87 GeV. The meaning of each curve is the same as in Fig. 2. The data are from Arndt [23].

tributions to the strength of the dressed vertex for $D_{33}[\Delta^*(J^P = \frac{3}{2}^-)] \rightarrow \pi\Delta(L = 0, S = \frac{3}{2})$. The effect of the $\pm 50\%$ variation in the magnitude of the $D_{33}[\Delta^*(J^P = \frac{3}{2}^-)] \rightarrow \pi\Delta(L = 0, S = \frac{3}{2})$ vertex becomes visible above $W \sim 1.5$ GeV and significantly large around $W = 1.6$ – 1.7 GeV. This is consistent with the existence of a resonance with a pole mass of $1577 - i113$ MeV in this partial wave within our 2016 model [16]. In contrast to the S_{31} and P_{33} cases, variations in this partial wave show a visible influence on $\pi^- p \rightarrow \pi^- \pi^0 p$ as well. The variation in the magnitude of the $D_{33}[\Delta^*(J^P = \frac{3}{2}^-)] \rightarrow \pi\Delta(L = 0, S = \frac{3}{2})$ vertex affects the invariant mass distributions at $W = 1.7$ GeV uniformly over the entire kinematically allowed range, but does not significantly change the shape of the distributions.

F_{37} : Figure 17 shows the sensitivity of the total cross sections and invariant mass distributions to the strength of the dressed vertex for $F_{37}[\Delta^*(J^P = \frac{7}{2}^+)] \rightarrow \pi\Delta(L = 3, S = \frac{3}{2})$. In our 2016 model [16], a single resonance with a pole mass of $1885 - i102$ MeV was found for the F_{37} partial wave, and indeed this partial wave shows a significant contribution to the cross sections around the energy region of this resonance pole (see Figs. 3 and 4). Varying the magnitude of the $F_{37}[\Delta^*(J^P = \frac{7}{2}^+)] \rightarrow \pi\Delta(L = 3, S = \frac{3}{2})$ dressed vertex by $\pm 50\%$ significantly affects the cross sections except $\pi^- p \rightarrow \pi^0 \pi^0 n$, and a reduction in this vertex strength is favored by the data. Conversely, we find that the cross sections are insensitive to variations in the other decay channels, $F_{37}[\Delta^*(J^P = \frac{7}{2}^+)] \rightarrow \pi\Delta(L = 5, S = \frac{3}{2})$ and $F_{37}[\Delta^*(J^P = \frac{7}{2}^+)] \rightarrow \rho N$. This observation seems consistent with the findings in Sec. IV of Ref. [14]. While reducing the magnitude of the $F_{37}[\Delta^*(J^P = \frac{7}{2}^+)] \rightarrow \pi\Delta(L = 3, S = \frac{3}{2})$

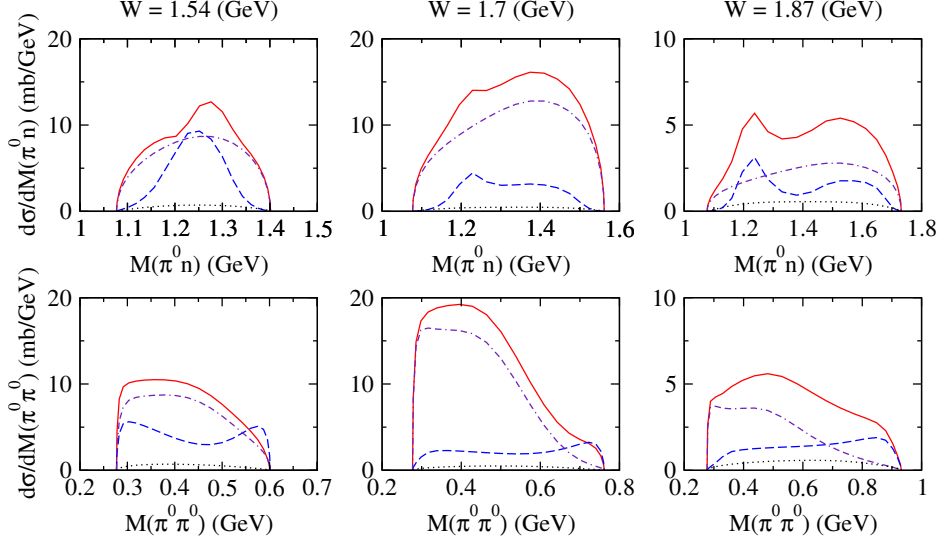


FIG. 12. Invariant mass distributions of $\pi^- p \rightarrow \pi^0 \pi^0 n$ at $W = 1.54, 1.70$, and 1.87 GeV. The meaning of each curve is the same as in Fig. 2.

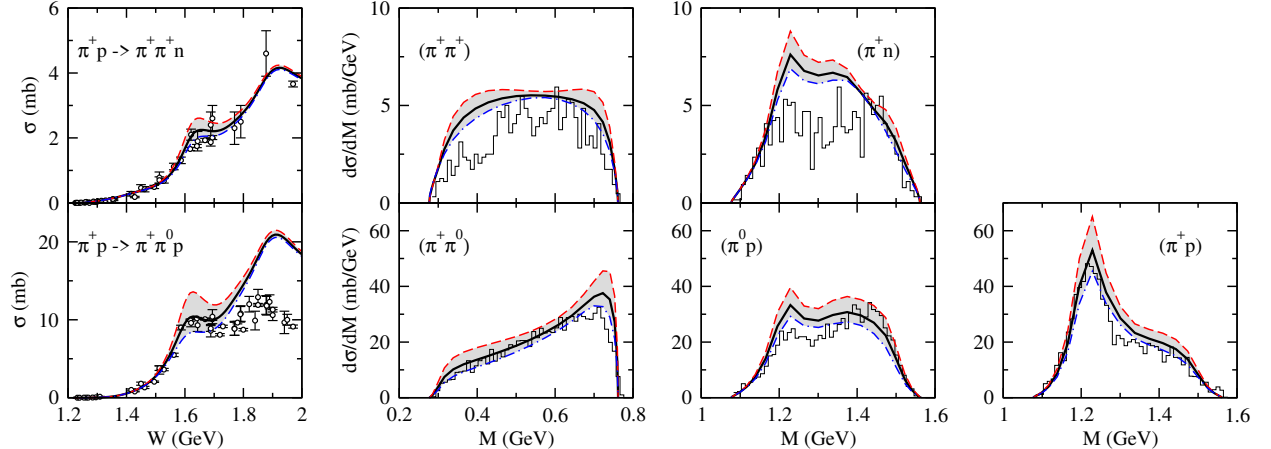


FIG. 13. Sensitivity of the cross sections to the $S_{31}[\Delta^*(J^P = \frac{1}{2}^-)] \rightarrow \pi\Delta(L = 2, S = \frac{3}{2})$ coupling. Leftmost column: Total cross sections. Remaining columns: Invariant mass distributions for the corresponding reactions at $W = 1.7$ GeV. The solid curves represent the full results, while the grey bands show the range obtained by allowing a 50% variation in the magnitude of the dressed vertices for $S_{31}[\Delta^*(J^P = \frac{1}{2}^-)] \rightarrow \pi\Delta(L = 2, S = \frac{3}{2})$ (the red dashed and blue dash-dot curves correspond to the results with $a_{MB(LS),N^*(I,J^P)} = 1.5$ and 0.5 , respectively). The data are taken from Refs. [9, 22, 23] and references therein.

vertex is favorable for reproducing the $\pi N \rightarrow \pi\pi N$ data, the resulting impact on the cross sections of other reactions, such as $\pi N \rightarrow MB$ ($MB = \pi N, K\Sigma$), through coupled-channel effects, can be compensated by adjusting the $F_{37}[\Delta^*(J^P = \frac{7}{2}^+)] \rightarrow \rho N$ couplings, which have a negligible influence on the $\pi N \rightarrow \pi\pi N$ reaction.

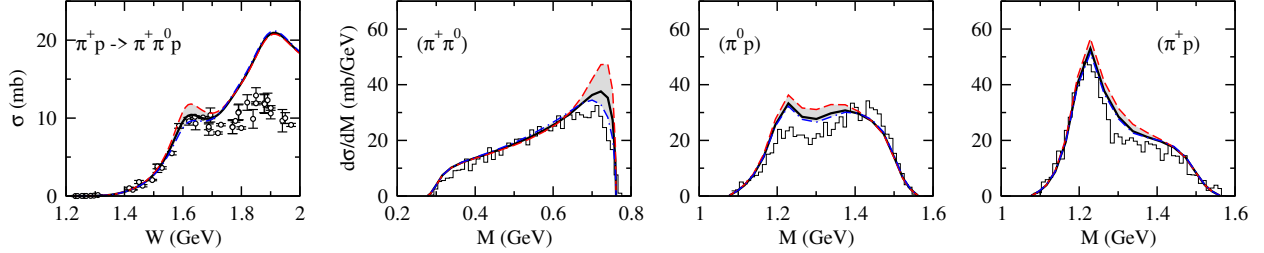


FIG. 14. Sensitivity of the cross sections to the $S_{31}[\Delta^*(J^P = \frac{1}{2}^-)] \rightarrow \rho N(L = 0, S = \frac{1}{2})$ coupling. Leftmost column: Total cross sections. Remaining columns: Invariant mass distributions for the corresponding reactions at $W = 1.7$ GeV. The solid curves represent the full results, while the grey bands show the range obtained by allowing a 50% variation in the magnitude of the dressed vertices for $S_{31}[\Delta^*(J^P = \frac{1}{2}^-)] \rightarrow \rho N(L = 0, S = \frac{1}{2})$ (the red dashed and blue dash-dot curves correspond to the results with $a_{MB(LS),N^*(I,J^P)} = 1.5$ and 0.5 , respectively). The data are taken from Refs. [9, 22, 23] and references therein.

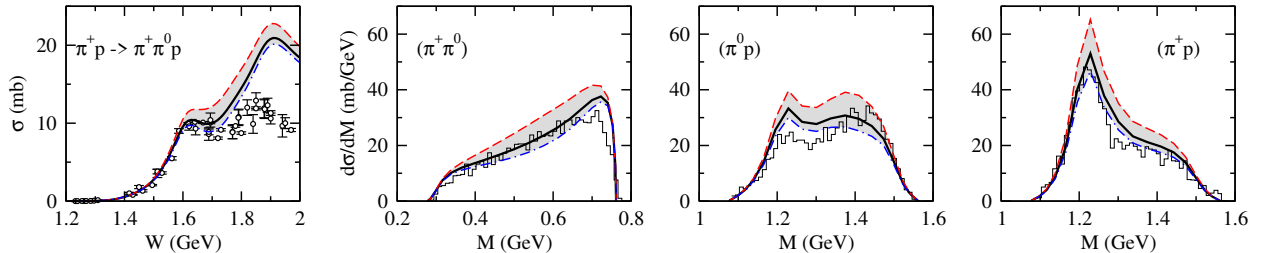


FIG. 15. Sensitivity of the cross sections to the $P_{33}[\Delta^*(J^P = \frac{3}{2}^+)] \rightarrow \pi\Delta(L = 1, S = \frac{3}{2})$ coupling. Leftmost column: Total cross sections. Remaining columns: Invariant mass distributions for the corresponding reactions at $W = 1.7$ GeV. The solid curves represent the full results, while the grey bands show the range obtained by allowing a 50% variation in the magnitude of the dressed vertices for $P_{33}[\Delta^*(J^P = \frac{3}{2}^+)] \rightarrow \pi\Delta(L = 1, S = \frac{3}{2})$ (the red dashed and blue dash-dot curves correspond to the results with $a_{MB(LS),N^*(I,J^P)} = 1.5$ and 0.5 , respectively). The data are taken from Refs. [9, 22, 23] and references therein.

2. Isospin $I = 1/2$ N^*

Next we investigate the sensitivity of the cross sections to the $I = 1/2$ N^* resonances. As we have seen from Fig. 4, above $W = 1.6$ GeV, D_{13} , D_{15} , and F_{15} have large contributions among the $I = 1/2$ partial waves.

D_{13} : Figure 18 shows the sensitivity of the total cross sections and invariant mass distributions to the strength of the dressed vertex for $D_{13}[N^*(J^P = \frac{3}{2}^-)] \rightarrow \rho N(L = 0, S = \frac{3}{2})$. We find that only the $\pi^- p \rightarrow \pi^- \pi^0 p$ reaction is sensitive to the variation in the magnitude of $D_{13}[N^*(J^P = \frac{3}{2}^-)] \rightarrow \rho N(L = 0, S = \frac{3}{2})$ vertex. The total cross sections at $W = 1.5$ – 1.7 GeV are sensitive to the variation of this vertex, which seems consistent with the existence of two resonances with pole masses of $1509 - i48$ MeV and $1702 - i148$ MeV³ found in our

³ The second pole is located in the complex energy plane slightly off the closest sheet to the physical real energy axis.

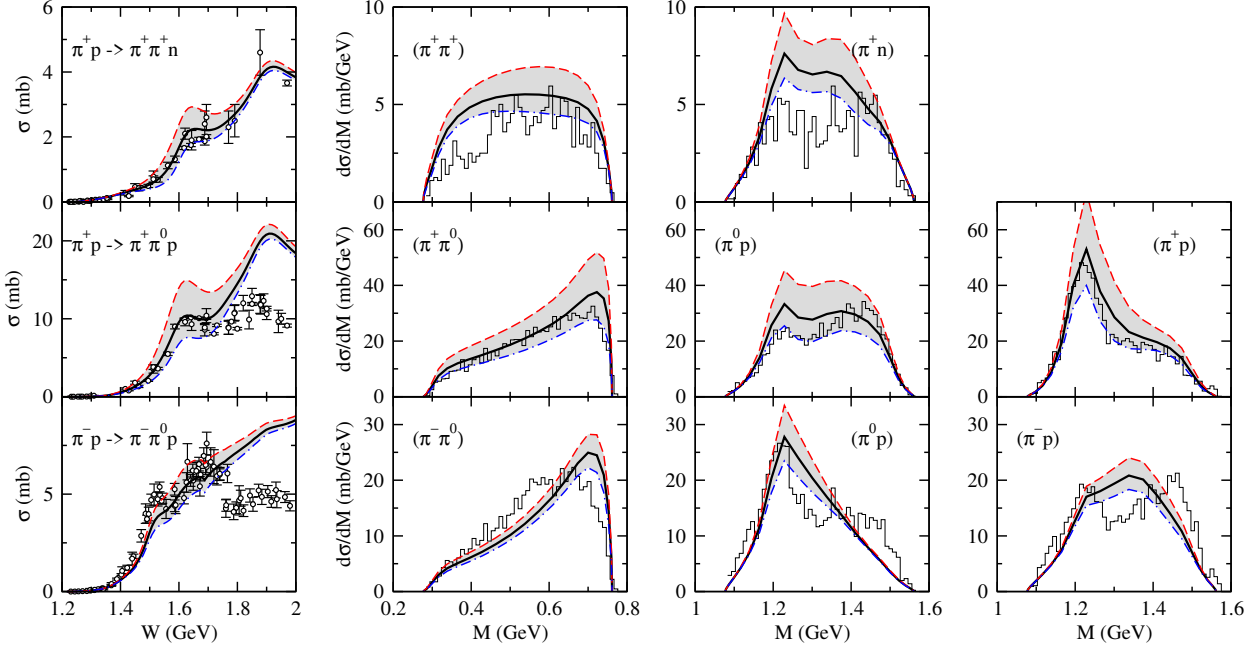


FIG. 16. Sensitivity of the cross sections to the $D_{33}[\Delta^*(J^P = \frac{3}{2}^-)] \rightarrow \pi\Delta(L = 0, S = \frac{3}{2})$ coupling. Leftmost column: Total cross sections. Remaining columns: Invariant mass distributions for the corresponding reactions at $W = 1.7$ GeV. The solid curves represent the full results, while the grey bands show the range obtained by allowing a 50% variation in the magnitude of the dressed vertices for $D_{33}[\Delta^*(J^P = \frac{3}{2}^-)] \rightarrow \pi\Delta(L = 0, S = \frac{3}{2})$ (the red dashed and blue dash-dot curves correspond to the results with $a_{MB(LS), N^*(I,JP)} = 1.5$ and 0.5 , respectively). The data are taken from Refs. [9, 22, 23] and references therein.

2016 model [16] for this partial wave. Similar to the $D_{33}[\Delta^*(J^P = \frac{3}{2}^-)] \rightarrow \pi\Delta(L = 0, S = \frac{3}{2})$ case, the variation in the magnitude of $D_{15}[N^*(J^P = \frac{3}{2}^-)] \rightarrow \rho N(L = 0, S = \frac{3}{2})$ vertex does not improve the shape of invariant mass distributions at $W = 1.7$ GeV.

D_{15} : Figure 19 shows the sensitivity of the total cross sections and invariant mass distributions to the strength of the dressed vertex for $D_{15}[N^*(J^P = \frac{5}{2}^-)] \rightarrow \sigma N(L = 3, S = \frac{1}{2})$. We note that the $\pi N \rightarrow N^* \rightarrow \sigma N$ process contributes only to the $\pi^- p \rightarrow \pi^+ \pi^- n$ and $\pi^- p \rightarrow \pi^0 \pi^0 n$ reactions. The results for the total cross sections and the invariant mass distributions at $W = 1.7$ GeV show that the 50% variation of the magnitude of this vertex has a significant effect around $W = 1.7$ GeV, which seems consistent with the existence of a resonance with a pole mass of $1651 - i68$ MeV found in our 2016 model [16] for this partial wave. Reducing the magnitude of the $D_{15}[N^*(J^P = \frac{5}{2}^-)] \rightarrow \sigma N(L = 3, S = \frac{1}{2})$ vertex seems to be favored by the data and will be key to resolving the overestimation of the cross sections around $W = 1.7$ GeV.

F_{15} : Figure 20 shows the sensitivity of the total cross sections and invariant mass distributions to the strength of the dressed vertex for $F_{15}[N^*(J^P = \frac{5}{2}^+)] \rightarrow \sigma N(L = 2, S = \frac{1}{2})$. This partial wave has a resonance with a pole mass of $1665 - i52$ MeV found in our 2016 model [16], and the 50% variation in the magnitude of this vertex shows a behavior quite similar to that of the $D_{15}[N^*(J^P = \frac{5}{2}^-)] \rightarrow \sigma N(L = 3, S = \frac{1}{2})$ case. Since the coupled-channel effects of the σN channel on the other πN reactions [$\pi N \rightarrow MB$

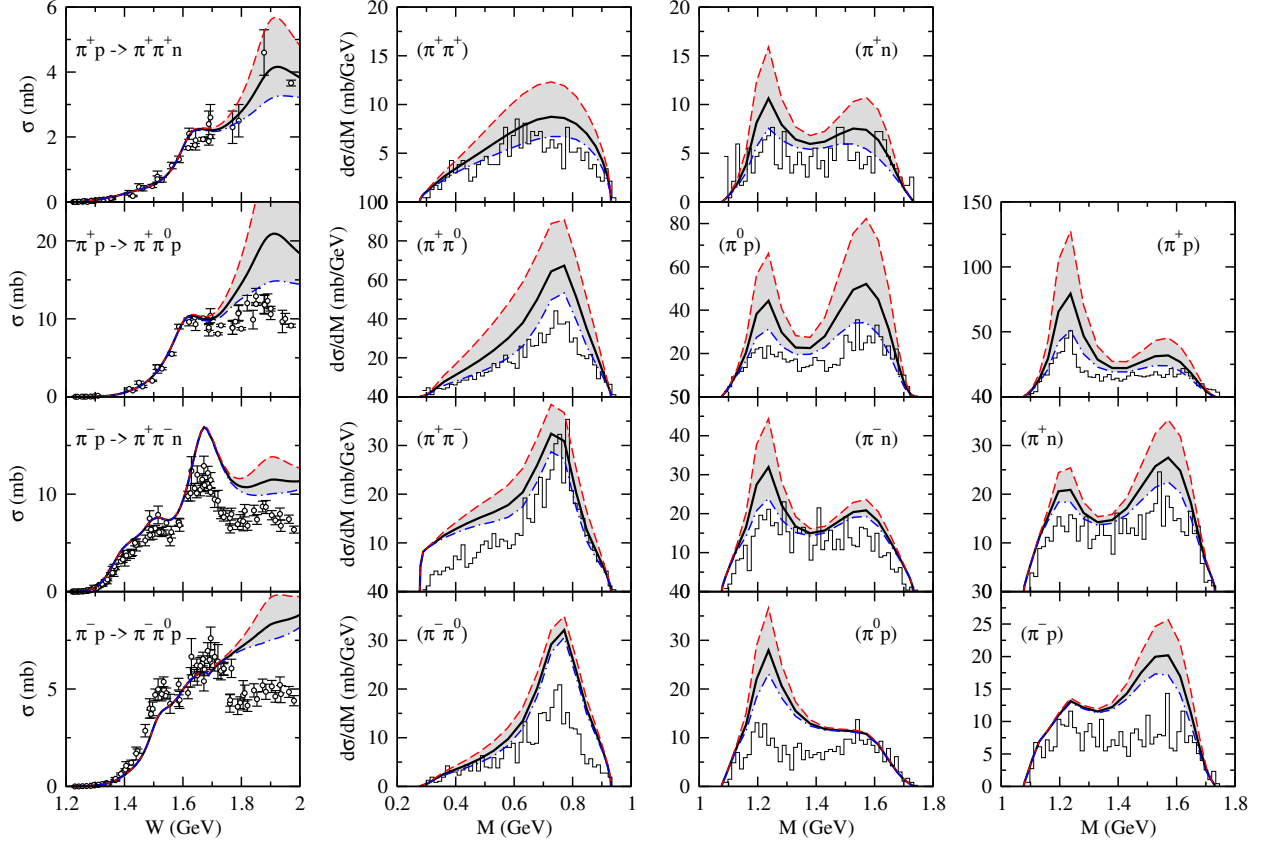


FIG. 17. Sensitivity of the cross sections to the $F_{37}[\Delta^*(J^P = \frac{7}{2}^+)] \rightarrow \pi\Delta(L = 3, S = \frac{3}{2})$ coupling. Leftmost column: Total cross sections. Remaining columns: Invariant mass distributions for the corresponding reactions at $W = 1.87$ GeV. The solid curves represent the full results, while the grey bands show the range obtained by allowing a 50% variation in the magnitude of the dressed vertices for $F_{37}[\Delta^*(J^P = \frac{7}{2}^+)] \rightarrow \pi\Delta(L = 3, S = \frac{3}{2})$ (the red dashed and blue dash-dot curves correspond to the results with $a_{MB(LS),N^*(I,J^P)} = 1.5$ and 0.5, respectively). The data are taken from Refs. [9, 22, 23] and references therein.

($MB = \pi N, \eta N, K\Lambda, K\Sigma$) are in general quite small, simply reducing the magnitude of both the $F_{15}[N^*(J^P = \frac{5}{2}^+)] \rightarrow \sigma N(L = 2, S = \frac{1}{2})$ and $D_{15}[N^*(J^P = \frac{5}{2}^-)] \rightarrow \sigma N(L = 3, S = \frac{1}{2})$ vertices is very promising to resolve the overestimation of the cross sections for $\pi^-p \rightarrow \pi^+\pi^-n$ around $W = 1.7$ GeV and for $\pi^-p \rightarrow \pi^0\pi^0n$ above $W = 1.6$ GeV.

IV. SUMMARY

We have extended our previous investigations of the $\pi N \rightarrow \pi\pi N$ reactions [9, 14] to predict the cross sections for these processes using the 2016 ANL-Osaka DCC model [16]. The model was constructed by fitting only the single-meson production data for πN and γN reactions: $\pi N, \gamma N \rightarrow \pi N, \eta N, K\Lambda, K\Sigma$. Thus, the results for $\pi N \rightarrow \pi\pi N$ presented here are pure predictions of the model, which serve to examine the extent to which the forthcoming data from J-PARC can be described. This study provides information for

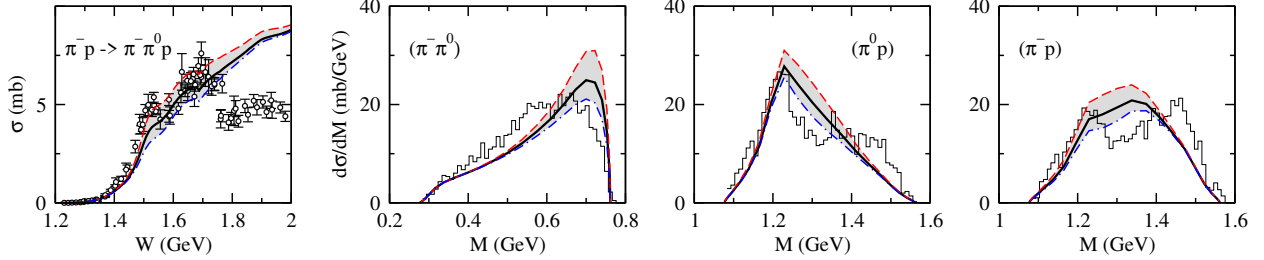


FIG. 18. Sensitivity of the cross sections to the $D_{13}[N^*(J^P = \frac{3}{2}^-)] \rightarrow \rho N(L = 0, S = \frac{3}{2})$ coupling. Leftmost column: Total cross sections. Remaining columns: Invariant mass distributions for the corresponding reactions at $W = 1.7$ GeV. The solid curves represent the full results, while the grey bands show the range obtained by allowing a 50% variation in the magnitude of the dressed vertices for $D_{13}[N^*(J^P = \frac{3}{2}^-)] \rightarrow \rho N(L = 0, S = \frac{3}{2})$ (the red dashed and blue dash-dot curves correspond to the results with $a_{MB(LS),N^*(I,J^P)} = 1.5$ and 0.5, respectively). The data are taken from Refs. [9, 22, 23] and references therein.

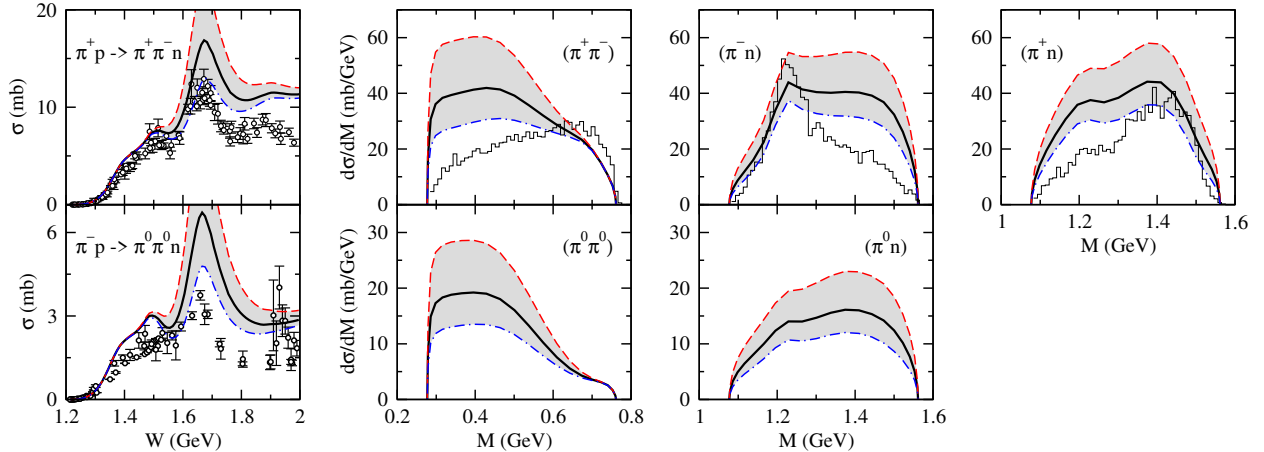


FIG. 19. Sensitivity of the cross sections to the $D_{15}[N^*(J^P = \frac{5}{2}^-)] \rightarrow \sigma N(L = 3, S = \frac{1}{2})$ coupling. Leftmost column: Total cross sections. Remaining columns: Invariant mass distributions for the corresponding reactions at $W = 1.7$ GeV. The solid curves represent the full results, while the grey bands show the range obtained by allowing a 50% variation in the magnitude of the dressed vertices for $D_{15}[N^*(J^P = \frac{5}{2}^-)] \rightarrow \sigma N(L = 3, S = \frac{1}{2})$ (the red dashed and blue dash-dot curves correspond to the results with $a_{MB(LS),N^*(I,J^P)} = 1.5$ and 0.5, respectively). The data are taken from Refs. [9, 22, 23] and references therein.

improving the extraction of nucleon resonances that have large decay widths to $\pi\pi N$ states via the quasi-two-body $\pi\Delta$, ρN , and σN channels.

We have presented the predicted total cross sections, invariant mass distributions, and angular distributions. Our results reasonably reproduce the overall features of the existing data even without including the $\pi N \rightarrow \pi\pi N$ reaction data in the fit, although discrepancies are observed, most notably a significant overestimation of the cross sections above $W \sim 1.65$ GeV. By examining the contributions from the $T^{\pi\Delta}$, $T^{\rho N}$, $T^{\sigma N}$, and T^{dir} processes and

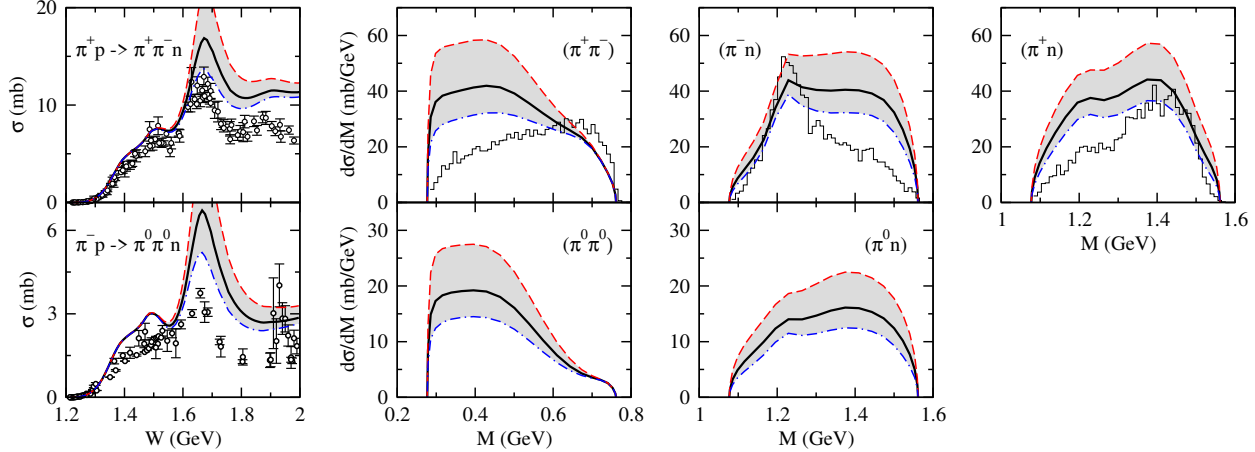


FIG. 20. Sensitivity of the cross sections to the $F_{15}[N^*(J^P = \frac{5}{2}^+)] \rightarrow \sigma N(L = 2, S = \frac{1}{2})$ coupling. Leftmost column: Total cross sections. Remaining columns: Invariant mass distributions for the corresponding reactions at $W = 1.7$ GeV. The solid curves represent the full results, while the grey bands show the range obtained by allowing a 50% variation in the magnitude of the dressed vertices for $F_{15}[N^*(J^P = \frac{5}{2}^+)] \rightarrow \sigma N(L = 2, S = \frac{1}{2})$ (the red dashed and blue dash-dot curves correspond to the results with $a_{MB(LS),N^*(I,J^P)} = 1.5$ and 0.5 , respectively). The data are taken from Refs. [9, 22, 23] and references therein.

individual partial waves, we have identified the primary sources of these discrepancies.

We have also investigated the sensitivity of the cross sections to the $\pi\Delta$, ρN , and σN couplings of nucleon resonances by varying the magnitudes of the fully dressed vertices for $N^* \rightarrow \pi\Delta, \rho N, \sigma N$ according to the prescription defined in Eq. (16). Through this investigation, we have identified the observables and energy regions where the high-mass resonances in the S_{31} , P_{33} , D_{33} , F_{37} , D_{13} , D_{15} , and F_{15} partial waves can be most effectively investigated.

We hope that the comprehensive predictions and sensitivity analyses presented in this paper will serve as a useful guide for future experiments. These insights are particularly relevant for the planning and analysis of the forthcoming measurements at J-PARC.

ACKNOWLEDGMENTS

The authors would like to thank Kyungseon Joo for useful discussions, and Shin Hyung Kim and Sangho Kim for providing information on the experiment at J-PARC. T.-S.H.L. is supported by the Office of Science of the U.S. Department of Energy under Contract No. DE-AC02-05CH112.

Appendix A: Sensitivity of angular distributions to the N^* states

In this Appendix, we present the sensitivity of the angular distributions to variations in the $\pi\Delta$, ρN , and σN couplings of N^* resonances. The results are displayed in Figs. 21–28. We focus on the same reactions and dressed vertices discussed in Sec. III C, where significant

effects on the total cross sections and invariant mass distributions were observed.

For invariant mass distributions, the cross section magnitudes are suppressed near the kinematic boundaries (maximum and minimum invariant masses) due to phase space effects, strictly vanishing at these limits. Consequently, it is generally difficult to observe sensitivity to variations in the $\pi\Delta$, ρN , and σN couplings in these edge regions. In contrast, angular distributions are not subject to such kinematic suppression at forward and backward angles ($\cos\theta \sim \pm 1$); thus, the distributions can exhibit significant variations even in these regions (see, e.g., Figs. 27 and 28, where we observe large changes in the magnitude of the distributions for the $\pi\pi$ pair at $\cos\theta \sim -1$). Furthermore, compared to the invariant mass distributions, the angular distributions appear to show more pronounced changes in shape, rather than just in overall magnitude (see, e.g., Fig. 25, where the $\pm 50\%$ variation of the magnitude of $F_{37}[\Delta^*(J^P = \frac{7}{2}^+)] \rightarrow \pi\Delta(L = 2, S = \frac{3}{2})$ coupling leads to the appearance or disappearance of a bump structure in the angular distributions for $\pi^+p \rightarrow \pi^+\pi^0p$). Therefore, to reliably extract N^* information from the $\pi N \rightarrow \pi\pi N$ reaction, it is highly desirable to have experimental data for both invariant mass and angular distributions.

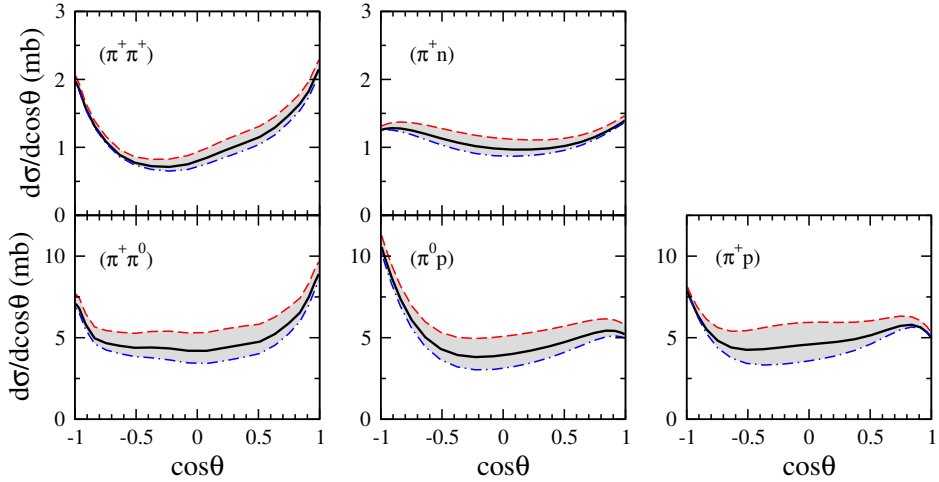


FIG. 21. Sensitivity of the angular distributions at $W = 1.7$ GeV to the $S_{31}[\Delta^*(J^P = \frac{1}{2}^-)] \rightarrow \pi\Delta(L = 2, S = \frac{3}{2})$ coupling. First row: $\pi^+p \rightarrow \pi^+\pi^+n$; second row: $\pi^+p \rightarrow \pi^+\pi^0p$. The scattering angle θ denotes the direction of the outgoing two-body subsystem indicated in parentheses. The solid curves denote the full results. The grey bands indicate the uncertainty resulting from a 50% variation in the $S_{31} \rightarrow \pi\Delta$ vertex magnitude (red dashed: $\times 1.5$; blue dash-dotted: $\times 0.5$).

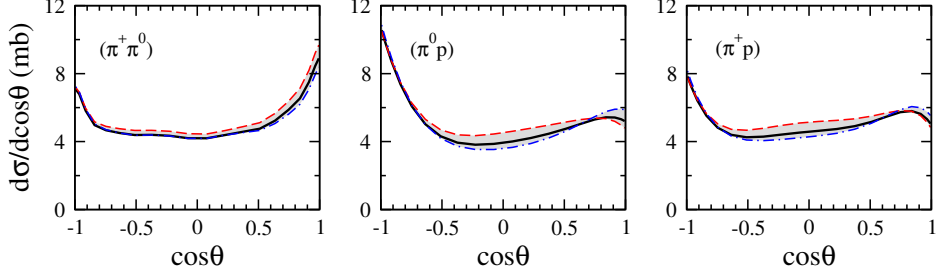


FIG. 22. Sensitivity of the angular distributions for $\pi^+ p \rightarrow \pi^+ \pi^0 p$ at $W = 1.7$ GeV to the $S_{31}[\Delta^*(J^P = \frac{1}{2}^-)] \rightarrow \rho N(L = 0, S = \frac{1}{2})$ coupling. The scattering angle θ denotes the direction of the outgoing two-body subsystem indicated in parentheses. The solid curves denote the full results. The grey bands indicate the uncertainty resulting from a 50% variation in the $S_{31} \rightarrow \rho N$ vertex magnitude (red dashed: $\times 1.5$; blue dash-dotted: $\times 0.5$).

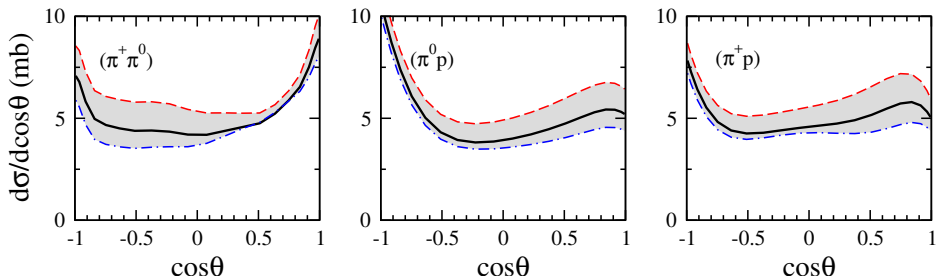


FIG. 23. Sensitivity of the angular distributions for $\pi^+ p \rightarrow \pi^+ \pi^0 p$ at $W = 1.7$ GeV to the $P_{33}[\Delta^*(J^P = \frac{3}{2}^+)] \rightarrow \pi \Delta(L = 1, S = \frac{3}{2})$ coupling. The scattering angle θ denotes the direction of the outgoing two-body subsystem indicated in parentheses. The solid curves denote the full results. The grey bands indicate the uncertainty resulting from a 50% variation in the $P_{33} \rightarrow \pi \Delta$ vertex magnitude (red dashed: $\times 1.5$; blue dash-dotted: $\times 0.5$).

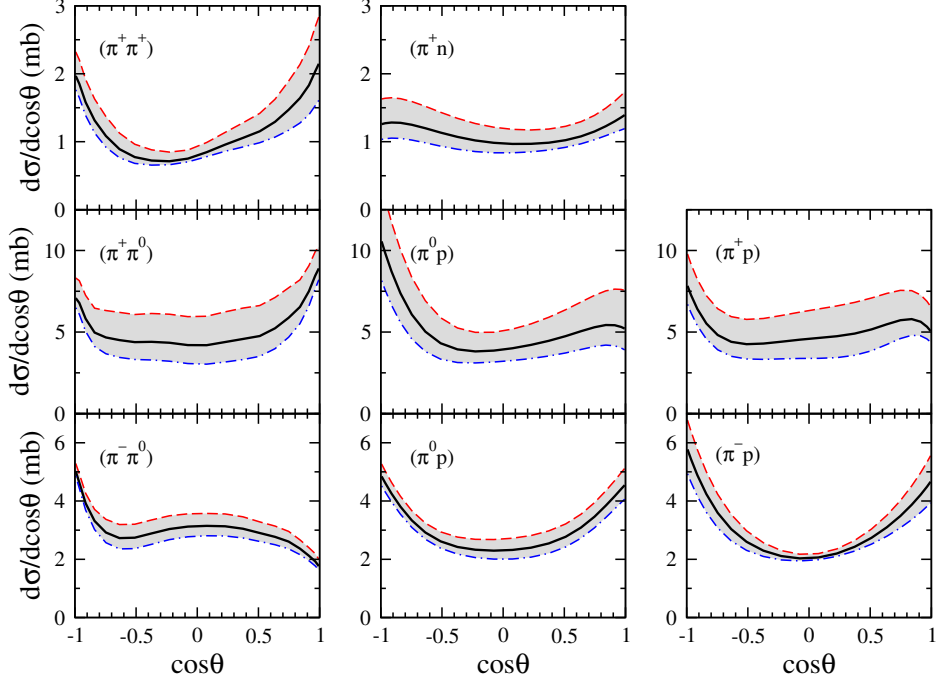


FIG. 24. Sensitivity of the angular distributions at $W = 1.7$ GeV to the $D_{33}[\Delta^*(J^P = \frac{3}{2}^-)] \rightarrow \pi\Delta(L = 0, S = \frac{3}{2})$ coupling. First row: $\pi^+p \rightarrow \pi^+\pi^+n$; second row: $\pi^+p \rightarrow \pi^+\pi^0p$; third row: $\pi^-p \rightarrow \pi^-\pi^0p$. The scattering angle θ denotes the direction of the outgoing two-body subsystem indicated in parentheses. The solid curves denote the full results. The grey bands indicate the uncertainty resulting from a 50% variation in the $D_{33} \rightarrow \pi\Delta$ vertex magnitude (red dashed: $\times 1.5$; blue dash-dotted: $\times 0.5$).

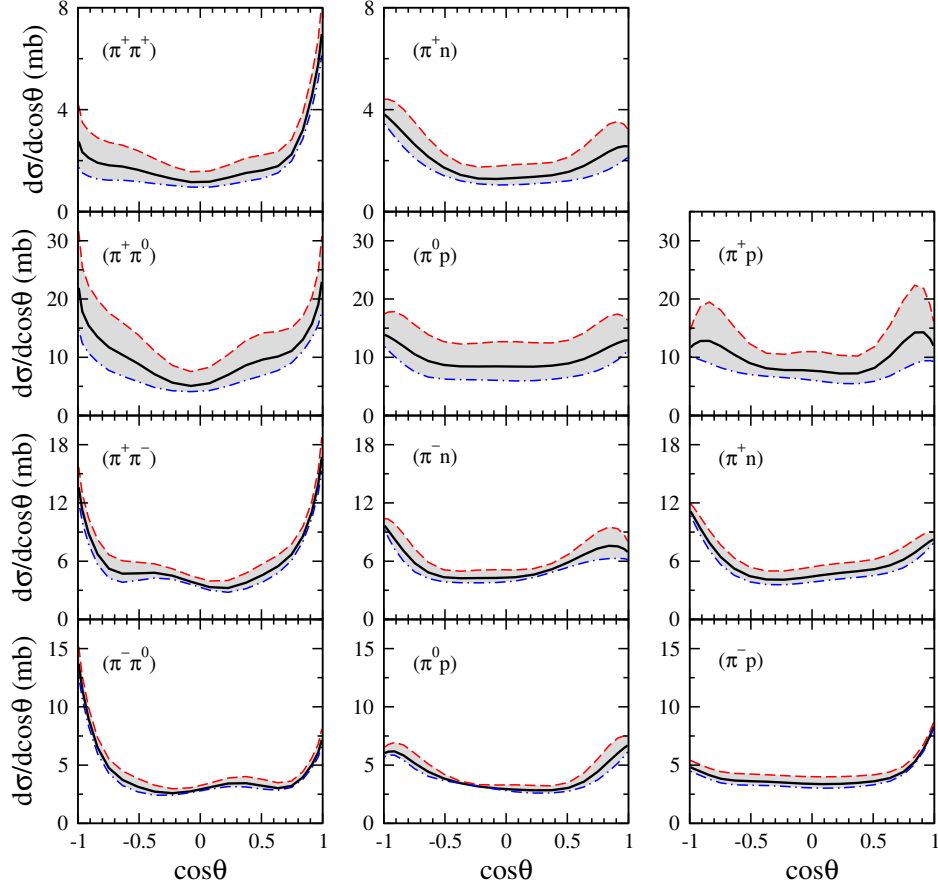


FIG. 25. Sensitivity of the angular distributions at $W = 1.87$ GeV to the $F_{37}[\Delta^*(J^P = \frac{7}{2}^+)] \rightarrow \pi\Delta(L = 3, S = \frac{3}{2})$ coupling. First row: $\pi^+p \rightarrow \pi^+\pi^+n$; second row: $\pi^+p \rightarrow \pi^+\pi^0p$; third row: $\pi^-p \rightarrow \pi^+\pi^-n$; fourth row: $\pi^-p \rightarrow \pi^-\pi^0p$. The scattering angle θ denotes the direction of the outgoing two-body subsystem indicated in parentheses. The solid curves denote the full results. The grey bands indicate the uncertainty resulting from a 50% variation in the $F_{37} \rightarrow \pi\Delta$ vertex magnitude (red dashed: $\times 1.5$; blue dash-dotted: $\times 0.5$).

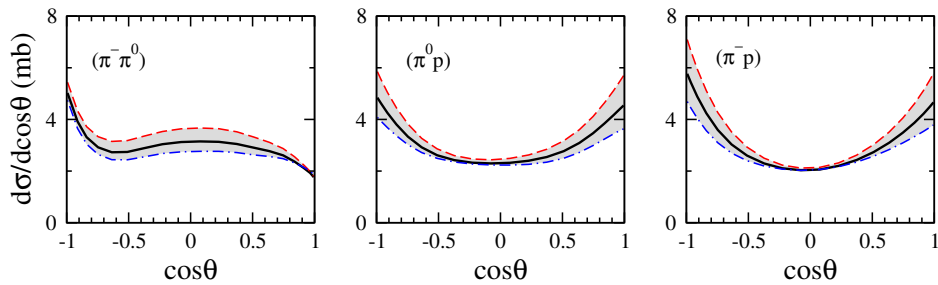


FIG. 26. Sensitivity of the angular distributions for $\pi^-p \rightarrow \pi^-\pi^0p$ at $W = 1.7$ GeV to the $D_{13}[N^*(J^P = \frac{3}{2}^-)] \rightarrow \rho N(L = 0, S = \frac{3}{2})$ coupling. The scattering angle θ denotes the direction of the outgoing two-body subsystem indicated in parentheses. The solid curves denote the full results. The grey bands indicate the uncertainty resulting from a 50% variation in the $D_{13} \rightarrow \rho N$ vertex magnitude (red dashed: $\times 1.5$; blue dash-dotted: $\times 0.5$).

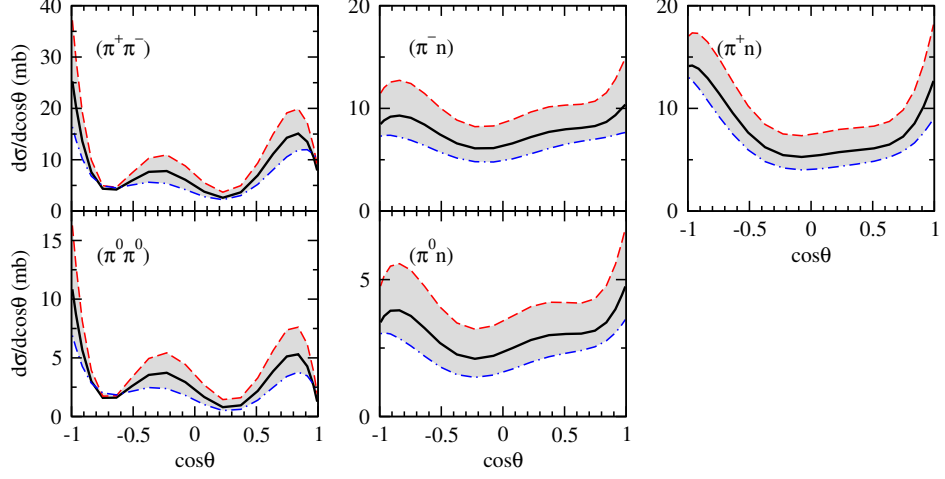


FIG. 27. Sensitivity of the angular distributions at $W = 1.7$ GeV to the $D_{15}[N^*(J^P = \frac{5}{2}^-)] \rightarrow \sigma N(L = 3, S = \frac{1}{2})$ coupling. First row: $\pi^- p \rightarrow \pi^+ \pi^- n$; second row: $\pi^- p \rightarrow \pi^0 \pi^0 n$. The scattering angle θ denotes the direction of the outgoing two-body subsystem indicated in parentheses. The solid curves denote the full results. The grey bands indicate the uncertainty resulting from a 50% variation in the $D_{15} \rightarrow \sigma N$ vertex magnitude (red dashed: $\times 1.5$; blue dash-dotted: $\times 0.5$).

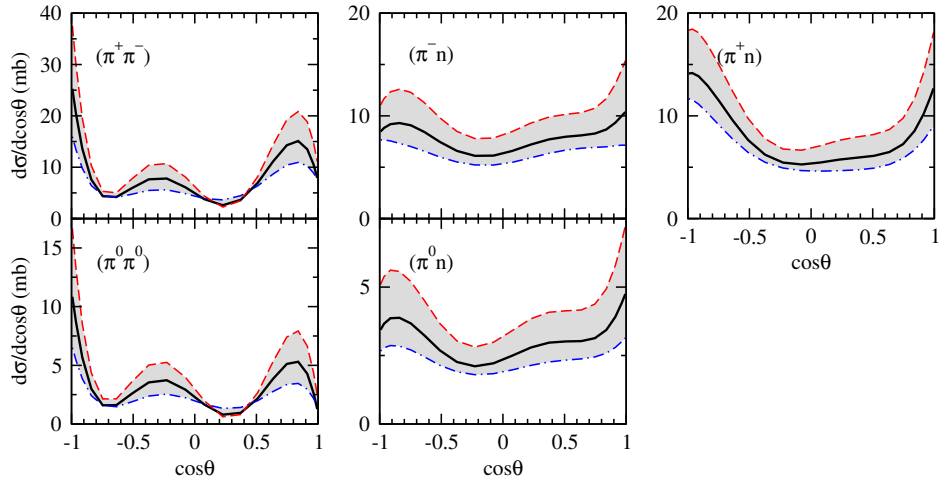


FIG. 28. Sensitivity of the angular distributions at $W = 1.7$ GeV to the $F_{15}[N^*(J^P = \frac{5}{2}^+)] \rightarrow \sigma N(L = 2, S = \frac{1}{2})$ coupling. First row: $\pi^- p \rightarrow \pi^+ \pi^- n$; second row: $\pi^- p \rightarrow \pi^0 \pi^0 n$. The scattering angle θ denotes the direction of the outgoing two-body subsystem indicated in parentheses. The solid curves denote the full results. The grey bands indicate the uncertainty resulting from a 50% variation in the $F_{15} \rightarrow \sigma N$ vertex magnitude (red dashed: $\times 1.5$; blue dash-dotted: $\times 0.5$).

[1] M. Döring, J. Haidenbauer, M. Mai and T. Sato, *Prog. Part. Nucl. Phys.* **46**, 104213 (2026).

[2] S. Prakhov *et al.* (Crystal Ball Collaboration), *Phys. Rev. C* **69**, 045202 (2004).

[3] J. Adamczewski-Musch *et al.* (HADES Collaboration), *Phys. Rev. C* **102**, 024001 (2020).

[4] A. V. Sarantsev, E. Klempt, K. V. Nikonov, T. Seifen, U. Thoma, Y. Wunderlich, P. Achenbach, V. D. Burkert, V. Mokeev, and V. Crede, *Phys. Rev. C* **112**, 015202 (2025).

[5] K. Hicks, H. Sako *et al.*, Measurements of $\pi N \rightarrow \pi\pi N$ and $\pi N \rightarrow KY$ at J-PARC (J-PARC E45), http://j-parc.jp/researcher/Hadron/en/pac_1207/pdf/P45_2012-3.pdf; K. Joo (private communications, 2025).

[6] T. Sato and T.-S. H. Lee, *Phys. Rev. C* **54**, 2660 (1996).

[7] A. Matsuyama, T. Sato, and T.-S. H. Lee, *Phys. Rep.* **439**, 193 (2007).

[8] B. Julia-Diaz, T.-S. H. Lee, A. Matsuyama, and T. Sato, *Phys. Rev. C* **76**, 065201 (2007).

[9] H. Kamano, B. Julia-Diaz, T.-S. H. Lee, A. Matsuyama, and T. Sato, *Phys. Rev. C* **79**, 025206 (2009).

[10] B. Julia-Diaz, H. Kamano, T. S. H. Lee, A. Matsuyama, T. Sato, and N. Suzuki, *Phys. Rev. C* **80**, 025207 (2009).

[11] H. Kamano, B. Julia-Diaz, T.-S. H. Lee, A. Matsuyama, and T. Sato, *Phys. Rev. C* **80**, 065203 (2009).

[12] N. Suzuki, T. Sato, and T.-S. H. Lee, *Phys. Rev. C* **82**, 045206 (2010).

[13] H. Kamano, S. X. Nakamura, T.-S. H. Lee, and T. Sato, *Phys. Rev. C* **88**, 035209 (2013).

[14] H. Kamano, *Phys. Rev. C* **88**, 045203 (2013).

[15] S. X. Nakamura, H. Kamano and T. Sato, *Phys. Rev. D* **92**, 074024 (2015).

[16] H. Kamano, S. X. Nakamura, T.-S. H. Lee, and T. Sato, *Phys. Rev. C* **94**, 015201 (2016).

[17] H. Kamano, *Few Body Syst.* **59**, 24 (2018).

[18] H. Kamano, S. X. Nakamura, T.-S. H. Lee, and T. Sato, arXiv:1909.11935v2 [nucl-th]; <https://www.phy.anl.gov/theory/research/anl-osaka-pwa/>, <https://www.rcnp.osaka-u.ac.jp/~anl-osk/>.

[19] H. Kamano, S. X. Nakamura, T.-S. H. Lee, and T. Sato, *Phys. Rev. C* **90**, 065204 (2014).

[20] H. Kamano, S. X. Nakamura, T.-S. H. Lee, and T. Sato, *Phys. Rev. C* **92**, 025205 (2015) [erratum: *Phys. Rev. C* **95**, 049903 (2017)].

[21] R. A. Arndt, W. J. Briscoe, I. I. Strakovsky, and R. L. Workman, *Phys. Rev. C* **74**, 045205 (2006); <https://gwdac.phy.gwu.edu>.

[22] D. M. Manley, R. A. Arndt, Y. Goradia, and V. L. Teplitz, *Phys. Rev. D* **30**, 904 (1984).

[23] R. A. Arndt (private communications, 2008).

[24] M. L. Goldberger and K. M. Watson, *Collision Theory* (John Wiley & Sons, New York, 1964).

[25] H. Kamano, M. Morishita and M. Arima, *Phys. Rev. C* **71**, 045201 (2005).

[26] H. Kamano and M. Arima, *Phys. Rev. C* **73**, 055203 (2006).